Heliyon 9 (2023) e12845

Contents lists available at ScienceDirect

Heliyon

journal homepage: www.cell.com/heliyon

Review article

Smart thermally responsive perovskite materials: Thermo-chromic application and density function theory calculation

Ning Jiang [a], Shuming Chen [a], Jintao Wang [a], Chenyang He [b], Kai Fang [b], Hanlin Yin [a], Yitong Liu [a], Ye Li [a,**], Duan Yu [b,*]

[a] College of Physics, Changchun University of Science and Technology, Changchun, Jilin Province, China
[b] State Key Laboratory on Integrated Optoelectronics, College of Electronic Science & Engineering, Jilin University, Changchun, Jilin Province, China

ARTICLE INFO

Keywords:
Thermochromic
Perovskite
Smart windows
DFT

ABSTRACT

With the continuous improvement of human's requirements for temperature control suitable for living, the energy consumption of electrical appliances such as air conditioners has become a major challenge in traditional architectural design. Generally, most of the solar energy passes through the glass to enter and exit the building, but the traditional glass can hardly control the light and heat energy, causing the indoor temperature to change dramatically with the environment. Therefore, it is more urgent to develop green and efficient smart windows. Perovskite is a temperature-adaptive material, which has the ability of phase transition and can adjust its band gap for thermochromic applications. In this work, we study the perovskite-based thermochromic smart window. As a new application of perovskite, a number of experiments have been carried out. However, there is still a lack of theoretical analysis on phase transition mechanisms and crystal structure prediction. Density functional theory (DFT) calculation is the most useful tool in optoelectronics, especially for perovskite crystal. Here, we extracted typical cases from published literature for analysis and comparison and summarized the crystal structure, electronic structure stability, interface engineering, and thermal characteristics employing DFT calculation We believe this work will pave the way for DFT application for the study of thermochromic perovskite.

1. Introduction

By October 2022, the world population has reached 7.988 billion, and this figure is expected to grow steadily in the next decade. The life supply required by the population expansion and the economic and industrial development has made the human demand for energy reach an unprecedented height. Due to the non-renewable nature of traditional energy (oil, coal, natural gas) and the warm house effect caused by carbon dioxide emissions from traditional energy supply, the energy system urgently needs to achieve decarbonization transformation [1,2]. According to statistics, the energy consumption of buildings accounts for 30–40% of the energy consumed in developed countries, which is much higher than the energy consumption of transportation and industry [3,4]. Half of building energy consumption comes from supply heating, ventilation and air-conditioning systems. It is predicted that building energy consumption will continue to rise in the next 20 years [5]. However, in buildings, windows are the most likely part to waste energy, so

* Corresponding author.
** Corresponding author.
E-mail addresses: liye@cust.edu.cn (Y. Li), duanyu@jlu.edu.cn (D. Yu).

https://doi.org/10.1016/j.heliyon.2023.e12845
Received 3 October 2022; Received in revised form 23 December 2022; Accepted 4 January 2023
Available online 6 January 2023

how to make green and energy-saving windows have become an urgent task. Smart window technology is expected to be the perfect answer to this problem. It is a new energy-saving technology that can reduce energy consumption by changing the transmittance and adjusting indoor solar radiation.

According to the different response modes, the smart window can be divided into electrochromic, thermochromic, photochromic and mechanical. At present, the development of electrochromic smart windows is relatively mature [6–9]. Some smart windows that use polymers and liquid crystal (LC) molecules as functional layers show great advantages in conversion speed and large-area, but such smart windows still need external excitation to work, and when the device area is expanded, the trigger device will consume more power [10,11]. This also shows that this smart window technology is more suitable for high-speed switching privacy windows or high-performance transparent displays than for energy-saving windows in buildings. Another kind of smart window using mechanical strain materials mainly changes the switchable optical characteristics caused by surface instability (wrinkle, bending). This material has been extensively studied because of its fast response, simple structure and low cost [12,13]. However, the durability of mechanical discoloration materials still exposes great problems, which also limits its industrial development. Some smart windows report the use of photochromic technology [14]. Photochromic materials can undergo a reversible color change when exposed to the light of a specific wavelength, and this color change principle does not require an additional trigger device. However, most organic photochromic materials cannot fade by simply removing ultraviolet light. Although inorganic photochromic materials can change color according to light intensity, their color changes are mainly colorless/white and blue [15]. The limitations of this material also limit its further research in the application of smart windows.

Based on previous research, we have made it clear that smart window technology suitable for wide application in buildings should comply with the following points:

1. The transition time between a transparent state and non-transparent state is very short, and the transition process is reversible;
2. The band gap and transmissivity of transparent and opaque states meet the actual needs;
3. The working mechanism does not require additional energy consumption;
4. The preparation technology is suitable for large-area production;
5. It has the potential to develop into multifunctional integrated devices.

Thermochromic (TC) is considered an alternative technology for smart windows that can meet the above conditions. The working mechanism of the TC smart window is to adjust its transmissivity according to temperature, and it is completely driven by materials, without an additional control system. These characteristics have aroused the great interest of researchers.

Because it is only driven by materials, thermochromic materials play a decisive role in smart window devices. Solar modulation efficiency (ΔT_{sol}), transmittance (T_{lum}), transition temperature (T_c) and transition time are the key indicators to measure the performance of TC materials. Table 1 lists the material selection and specific characteristics of recent work related to thermochromic smart windows. Vanadium dioxide (VO_2) is a relatively early and mature thermochromic material [16–22]. It can realize reversible phase transition between metal and insulator at specific temperature. Therefore, VO_2 becomes an attractive candidate material for smart windows. This phase transition makes it an attractive candidate material for smart windows. However, the absorption range of this material is only near infrared ($\lambda > 900$ nm), which will cause its ΔT_{sol} is low. And its high Tc, high manufacturing cost, short life and other problems also make it very difficult to further develop. In order to solve the problems exposed by VO_2 as a thermochromic smart window material, researchers have conducted research on other candidate materials. Some hydrogel materials, such as Poly (N-isopropylacrylamide) (PNIPAm) and hydroxypropyl cellulose (HPC), have attracted wide attention because their transmissivity will change significantly with the change from hydrophilicity to hydrophobicity (250–1800 nm) [16,23–27]. For example, Kunming Li et al. recently reported the work of smart window. They used sodium dodecyl sulfate (SDS) and potassium tartrate hemihydrate to prepare hydrogel material as a functional layer, and used indium tin oxide as an electric heating layer [28]. The shielding transmissivity of visible light and near-infrared light of this smart window at 25 °C reached 88.3% and 85.4% respectively. The transmissivity at 550 nm after power on exceeded 70%, and the Tc of the hydrogel smart window using different components was 28–35 °C. T_c close to room temperature indicates that this kind of smart window is suitable for daily use. However, due to the liquid phase nature of hydrogels, they need to be extremely tightly encapsulated, and if material leakage occurs in the process of use, the efficiency of devices will fall precipitously. Therefore, we still need to find a kind of thermochromic material with excellent performance and easy packaging.

Table 1
Performance comparison of three materials.

Materials	Structure	ΔT_{sol}	T_{lum}	Transition temprature	Transition time	Ref.
VO_2	$ZrO_2/VO_2/ZrO_2$	10.20%	55.80%	68 °C	–	[42]
	VO_2/ZnO	19.30%	55.90%	~50 °C	–	[43]
	$Zn_2V_2O_7$-VO_2	10.70%	72.10%	49 °C	–	[44]
	VO_2-W_{dope}/ZnO	15.31%	59.57%	37 °C	–	[45]
Hydrogels	PNIPAm	79.76%	82.79%	32 °C	–	[46]
	HPC	19.40%	91.30%	–	–	[47]
Perovskite	$MAPbI_{3-x}Br_x$	15%	25%	~40 °C		[48]
	$MAPbI_{3-x}Cl_x$	23.70%	85.20%	40.1 °C	1~4min	[49]
	CWO/perovskite/Low-E	17.50%	65.70%	43 °C	8.3min	[50]

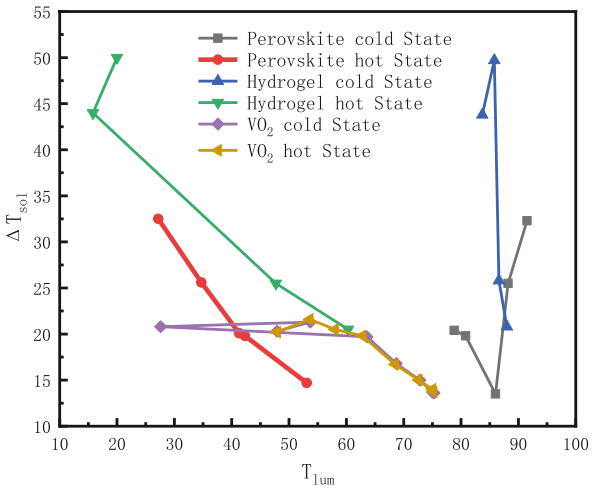

Fig. 1. Comparison of optical properties of treated $MAPbI_3$ perovskite with VO_2 and hydrogel.

Perovskite materials have attracted extensive attention due to their excellent photovoltaic properties in terms of band gap adjustability, absorption coefficient, carrier mobility, etc. And it has low manufacturing cost, high defect tolerance and easy packaging. In addition, in the photovoltaic field, the photoelectric conversion efficiency (PCE) of the perovskite solar cell is close to that of the silicon solar cell (about 25%), which means that the perovskite TC smart window is very likely to develop into a multi-functional integrated device. In 2018, Jia Lin et al. reported a thermochromic smart window using $CsPbIBr_2$ inorganic halide perovskite [29]. The reversible change of visible light transmittance from 35.4% to 81.7% was achieved through the water mediated phase transition property of the material itself. And the dark perovskite phase of this device can produce the PCE of 7%. After repeated phase transition period, the performance of the device does not decline significantly, which indicates its excellent device stability. This work combines smart windows and solar cells to achieve both energy saving and power generation in one device, which is a very meaningful exploration. However, in addition to the extremely high low-temperature phase transmittance and 7% high-temperature phase photoelectric conversion efficiency, the devices they fabricated also exposed the problems of high phase T_c (105 °C) and long transition time (25 h). In 2019, Y. Zhang et al. Successfully prepared smart window devices with low-temperature phase transmittance of 91% by adjusting the solution ratio and spin coating rate in the manufacturing process of $MAPbI_3$ perovskite, and the transition time was less than 5min [30]. By changing the ratio of PbI_2 and MA and the spin coating rate, the light transmittance under high-temperature phase can change between 34.3% and 59.6%, and the solar modulation ability can change between 12.7% and 25.5%.They also measured the T_c lag of perovskite smart windows, and the results showed that the T_c depended on the relative humidity in the environment. When the relative humidity is less than 60%, the T_c can be lowered to below 43 °C. However, although this work has made very obvious progress in reducing the T_c, 43 °C is still higher than the actual indoor temperature, so we still need to invest more energy in this direction. Another highlight of this work is that they compared the solar modulation efficiency and transmittance of high/low-temperature phases of thermochromic smart windows using $MAPbI_3$ perovskite, VO_2, and hydrogels, respectively. As shown in Fig. 1, the treated $MAPbI_3$ perovskite shows better optical properties than VO_2 and Hydrogel.

Therefore, we will focus on reviewing and discussing the work related to perovskite thermochromic smart window (PTSW). In addition, because the density functional theory (DFT) simulation shows extremely reliable accuracy in revealing the reaction mechanism, predicting new materials, etc., and has been widely used in the perovskite photovoltaic field [31–41], we will also summarize and discuss its application in the thermochromic field. In short, this review is divided into three parts: In the first part, we introduce DFT simulation and its specific functions in detail; In the second part, we reviewed the recent work on PTSW and put forward our analysis and suggestions; Finally, we summarized the content of the article and put forward our own views on the future development of PTSW.

2. DFT simulation

The ground-state electronic structure and nuclear repulsion in a solid material determine its lattice constant, cohesive energy, band structure, surface reactivity, thermochemistry, rate constant, and other physical and chemical properties, which are based on the Schrödinger equation of Born-Oppenheimer approximation [51]. At present, the main method to solve the Schrodinger equation is density functional theory (DFT) based on the Kohn-Sham equation. After decades of development, the density functional has undergone the upgrading from the first-generation local spin density approximation (LSDA) to the second generation generalized gradient approximation (GGA) and the third generation functional (meta GGA) using spin kinetic energy density or spin density Laplacian. DFT simulation is based on the interaction between the atomic nucleus and electrons in the material, which directly predicts and calculates the material properties without relying on empirical models or fitting parameters. In recent years, DFT calculations have been increasingly used in structural simulations, energy band calculations, and electronic structure analysis [8,9,52–55]. Compared

with experiments, DFT calculation can better explain the reaction mechanism, predict new materials, and save experimental costs. Here, we discuss the possible application of DFT computational simulation in the field of thermochromic perovskite smart windows, and review and analyze the recent work from four aspects: crystal structure, electronic structure, interface engineering, and thermoelectric performance.

2.1. Crystal structure

In the process of thermochromism, the crystal structure of perovskite will change from the orthorhombic phase to the cubic phase. We can simulate this phase transition process through DFT, and even predict the temperature of the phase transition point of the new material by reverse inference, to save the experimental cost. In addition, crystal structure stability is also an important property that determines the cycle life of smart window devices. We can judge the structural stability of materials by calculating cohesive energy, formation energy, Gibbs free energy and phonon spectrum. In this part, we review some cases of phase transition simulation and introduce the above four methods to judge structural stability.

2.1.1. Thermochromic phase transition

The thermochromic process of perovskite is usually accompanied by the change from a low-temperature transparent phase to a high-temperature output phase [49,56]. For example, organic halide perovskite generally induces phase transition by hydration, while inorganic perovskite materials will change from orthogonal phase to cubic phase at a certain temperature. DFT simulation can realize the visualization of this phase transition process, that is, simulate the crystal structure and changes under specific temperature or pressure changes. As shown in Fig. 2, the phase transition process of $CsPbI_3$ is shown. The gray atom represents the Cs^+ ion at position A, and the orange represents the PbI_6 cubic octahedron. This material can change between the orthogonal phase and cubic phase by heating and cooling.

Recently, Jonathon S. Bechtel et al. conducted Monte Carlo simulation on the basis of DFT, showing us a method to reproduce the phase transformation process of materials [57]. They constructed an anharmonic Hamiltonian to describe the low potential energy part of $CsPbBr_3$, and verified it with the crystal deformation data calculated by DFT simulation. Then they performed Monte Carlo simulation based on Hamiltonian to reproduce the orthogonal-tetragonal-orthogonal phase transition process of $CsPbBr_3$ and other halide perovskite, it also proves the importance of non-resonant excitation in improving the phase transition stability of materials. Fig. 3a shows the thermodynamic average strain order parameters calculated using the anharmonic vibration Hamiltonian. Moreover, Fig. 3b shows the lattice distortion and atomic displacement parameter (ADP) at different temperatures. This reparameterized anharmonic vibrational Hamiltonian shows a more stable stability range for the tetragonal β phase. The phase transition in inorganic halide perovskite is usually described by the collective tilt mode of the halide sublattice. Base on the anharmonic vibration Hamiltonian, they explored the local environment of the octahedron tilt shown in Fig. 4. As shown in Fig. 4a, they first applied the Kabsch algorithm to each octahedron to extract Euler angles to find the best rotation matrix that minimizes the square distance between rotating and non-rotating octahedrons. Then, the rotation matrix is decomposed into the basic external Euler angle $R_x(\varphi)$、$R_y(\theta)$ and $R_z(\psi)$, which Represents the rotation around the Cartesian x, y, and z axes, respectively. Fig. 4 (b) shows a histogram of individual octahedral rotations in each phase. In the orthogonal phase, there are two peaks in the distribution of each Euler angle. In these simulations, in-phase rotation occurs around the z-axis, and in-phase rotation occurs along the x and y-axes. The octahedral rotation between the orthogonal phase and the tetragonal phase has a gradual process because the double peaks along x and y combine to form a single peak centered on zero in the tetragonal phase. Similarly, when heated to the cubic phase, the in-phase tilt peaks merge into a peak centered on 0. In Fig. 4 (c), the distribution is shown as a function of temperature, where the average rotation angle can be used as an order parameter through two phase transitions. In the cubic to tetragonal transition, the tilts along x and y go to 0, while the tilts along z only go to zero during the tetragonal to cubic transition.

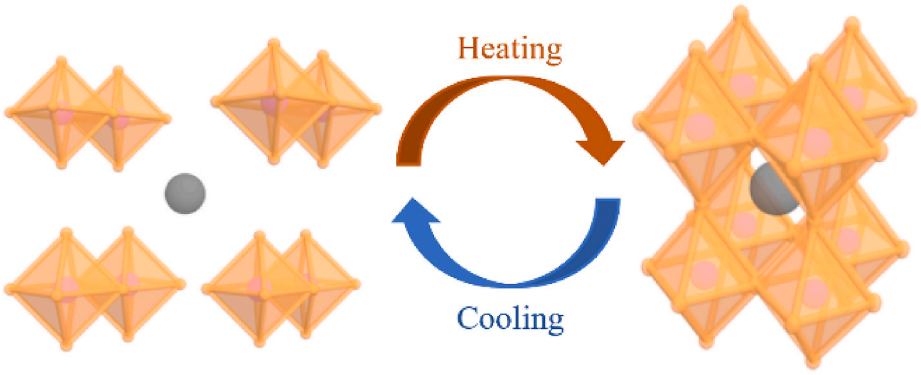

Fig. 2. The phase change of thermochromic perovskite (gray atom represents the Cs^+ ion at position A; the orange represents the PbI_6 cubic octahedron). (For interpretation of the references to color in this figure legend, the reader is referred to the Web version of this article.)

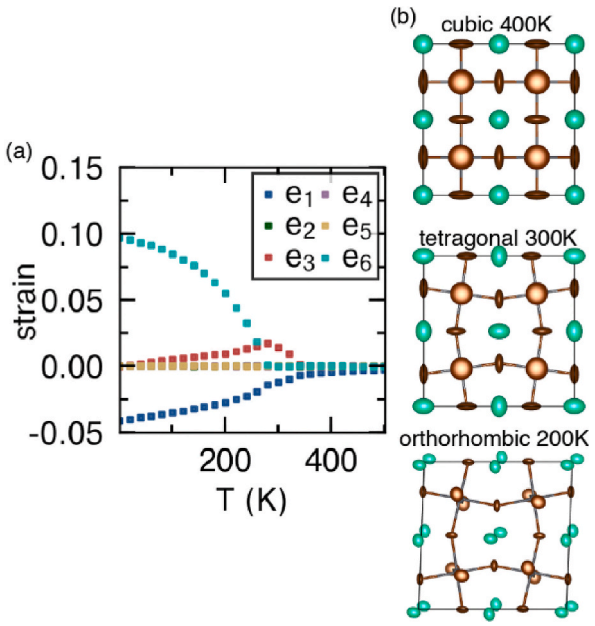

Fig. 3. (a) Thermodynamic average strain order parameter. (b) Average structure and atomic displacement parameters (ADP) at different temperatures.

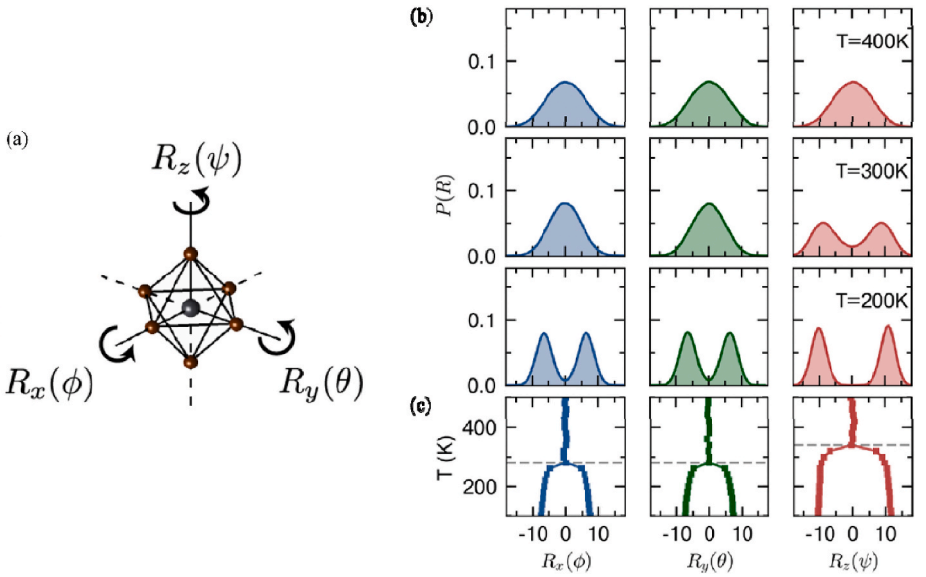

Fig. 4. (a) The extrinsic Euler rotations about the x, y, and z rotation axes.(b) Rotation of a single octahedron at different temperatures. (c) The functional relationship between rotation angle in three directions and temperature.

2.1.2. Structural stability

Based on DFT simulation, the structural stability of crystals can be judged by calculating their cohesive energy, formation energy, Gibbs free energy and phonon spectrum. Cohesive energy refers to the interaction force or electrostatic force between atoms or molecules in the system, so the magnitude of cohesive energy is often used to judge the structural stability. The cohesive energy formula is as follows:

$$E_{CO} = \frac{E(A_mB_n) - mE(A) - nEB}{m+n} \tag{1}$$

where E_{co} is the internal concentrated energy, E represents the energy, and A and B are two kinds of isolated atoms. The m and n are the number of atoms of A and B, respectively. E (A_mB_n) is the energy of the compound composed of atoms A and B. The absolute value of

Table 2
The cohesive energies of $SrMoO_3$ perovskite doped with different amounts of Mg.

SrMo1-xMgxO3	a (Å)	V (Å)	B (GPa)	Ecoh (eV/atom)
x = 0.0	3.9945	63.737	183.49	–
	3.621	47.477	185.18	−1.636
	3.972	62.665	–	–
	3.9762	62.869	–	–
x = 0.1	3.8964	59.18	136.07	–
	3.556	44.964	148.28	−1.62
	3.9695	62.546	–	–
x = 0.2	3.8634	57.665	144.14	–
	3.5721	45.576	151.11	−1.6317
	3.9649	62.332	–	–
x = 0.3	3.844	56.806	148.29	–
	3.589	46.23	152.07	−1.629
x = 0.4	3.7952	54.665	160.78	–
	3.5922	46.346	157.37	−1.267

the cohesion energy is usually positively correlated with structural stability. Recently, Khandaker Monower Hossain et al. published a report on the effect of magnesium doping on the physical properties of $SrMoO_3$ perovskites [58]. $SrMoO_3$ perovskite is a relatively common perovskite material, and its electronic, structural and physical properties are widely studied topics in materials science. They calculated the cohesive energies of $SrMoO_3$ perovskite doped with different amounts of Mg, as shown in Table 2. The calculation results show that Mg doping only slightly weakens the cohesive energy of the material, which ensures the structural stability of the material they studied.

Formation energy is the energy absorbed or released in the process of forming compounds. The formation energy formula is as follows:

$$E_f = E(A_mB_n) - mE(A) - nE(B) \tag{2}$$

where E_f is the energy of the elements A and B to form A_mB_n. The m and n are the number of elements A and B, respectively. The absolute value of the formation energy is usually positively correlated with structural stability. Although similar to the cohesive energy formula, E here is not the energy of isolated atoms but the energy of constituent elements in the standard state. Because compounds are mostly composed of elements rather than isolated atoms, it is more stable to use formation energy for structure prediction than cohesive energy. Recently, T Ghrib et al. published a study on the optical and thermoelectric properties of lead-free double perovskite $K_2Ti(Cl/Br)_6$ material [35]. They found that the direct band gap of K_2TiCl_6 is 2.80 eV and that of K_2TiBr_6 is 2.1 eV. The absorption maxima from visible to ultraviolet range from 2.5 eV to 4 eV, which suggests that they can be used as light-absorbing materials for solar cells. They demonstrated the structural stability of the two materials by calculating the formation energy of $K_2Ti(Cl/Br)_6$. The calculated formation energies of K_2TiCl_6 and K_2TiBr_6 are −2.40 eV and −2.25 eV, respectively.

Gibbs free energy refers to the ability of the system to do non volume work in the thermodynamic process under certain temperature and pressure conditions, so it can also be used to judge the structural stability. Gibbs free energy is affected by temperature(T), pressure(P), volume(V), system internal energy(E) and entropy(S), and its calculation formula is as follows:

$$G = E + PV - TS \tag{3}$$

Recently, Atsushi Suzuki et al. calculated the Gibbs free energy of halide perovskite $FAPbI_3$ doped with different alkali metals (Li, Na, K, or Rb) using DFT simulation calculations [59]. As shown in Fig. 5 (a), the addition of alkali metals reduces the Gibbs free energy of perovskite, thus making the structure more stable. Moreover, it can be seen from Fig. 5 (b) that the Gibbs free energy of perovskite decreases with the increase of lattice constant within a certain range.

The phonon spectrum is a good starting point for studying the stability properties of materials. It can be divided into two frequencies: optical wave and acoustic wave. When the phonon spectrum is all above 0, it indicates that the material does not appear virtual frequency, that is, the material is relatively stable. For example, Tarik ouahrani et al. used DFT simulation to calculate the phonon spectrum and projection dynamic density (PDOS) of $CsScO_3$ perovskite under 0 and 40 GPa pressure in their reports on the influence of pressure on the lattice vibration and electronic properties of $CsScO_3$ perovskite [60]. As shown in Fig. 6, there is no virtual frequency in the phonon spectrum, indicating that the perovskite material can maintain the stability of the orthogonal structure within 40Gpa. This conclusion is consistent with their experimental results, and also proves the accuracy of DFT simulation. The density of states diagram shows that Ce^{3+}, $Sc^{3+}$and O^{2-}ions play a leading role in the low frequency (<200 cm^{-1}), medium frequency (200-350 cm^{-1}) and high frequency (>350 cm^{-1}) vibration parts respectively. The change of pressure has a relatively obvious impact on the middle and high frequency motion, which can also be said that the increase of pressure mainly limits the internal vibration of the ScO_6 octahedron.

2.2. Electronic structure

Electronic structural properties play a crucial role in the performance of batteries and smart window devices [34,36,39,61–64]. The main goal of DFT simulation is to use electron density instead of the wave function as the basic quantity of calculation. Therefore,

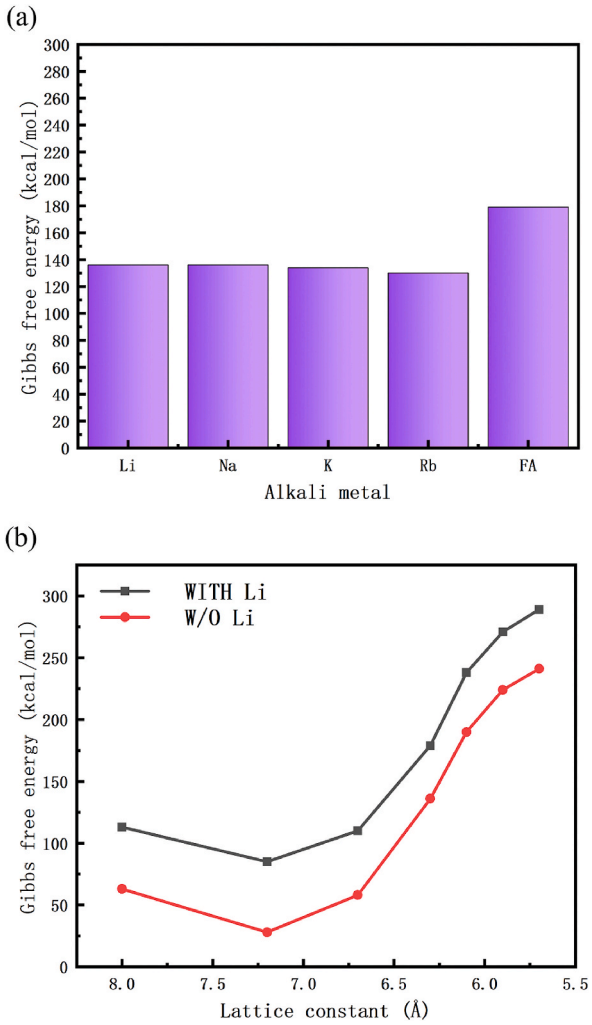

Fig. 5. (a) Gibbs free energy of $FAPbI_3$ doped with different alkali metals. (b) Effect of lattice coefficient on Gibbs free energy before and after Li doping.

electronic structure characteristics such as charge distribution, energy band structure, and density of states (DOS) of the device can be obtained through DFT calculation, to measure the performance of the device.

2.2.1. Charge distribution

The distribution of charges in the electronic structure and the chemical environment of the atoms are difficult to measure experimentally but can be calculated by DFT simulations, which is an advantage of DFT simulations compared to traditional experiments [34,65,66].

Recently, June Ho Lee et al. published work on spin-polarized bandgap materials for smart windows [67]. They chose the A_2CuX_4 perovskite and adjusted the element selection at the A positions. Among them, they calculated the partial charge distribution of Rb_2CuBr_4 using DFT simulations. As shown in Fig. 7a, the valence band maximum (VBM) states of the valence band of Rb_2CuBr_4 is mainly distributed between the $3d_{z2\text{-}x2}$ and $3d_{y2\text{-}x2}$ orbitals of Cu and the p-orbital of Br. The d-orbital of Cu based on the solid line part of Br bond shows the major impact, indicating the existence of the Jahn-Teller amentiferous distortion. The spatial distribution of VBM states is modified when the A-bit is switched from Rb to K (Fig. 7b) and from Rb to Cs(Fig. 7c). For smaller K ions, the VBM states in the d orbitals of Cu increase, which are aligned towards the longer bonded Br (Fig. 7b, red area). This change indicates a weakening of the Jahn-Teller amentiferous distortion and an increase in band dispersion with increasing orbital overlap. In contrast, for large Cs ions, the VBM state in the d orbital of Cu aligned towards long bonds Br decreases (Fig. 7c, blue area). As a result, the band dispersion is decreased by the reduced orbital overlap. These results show that the overlap of the orbits between the d-orbital of Cu and p-orbital of Br leads to the change of the energy band dispersion, so the A-bit effect on the band gap will occur.

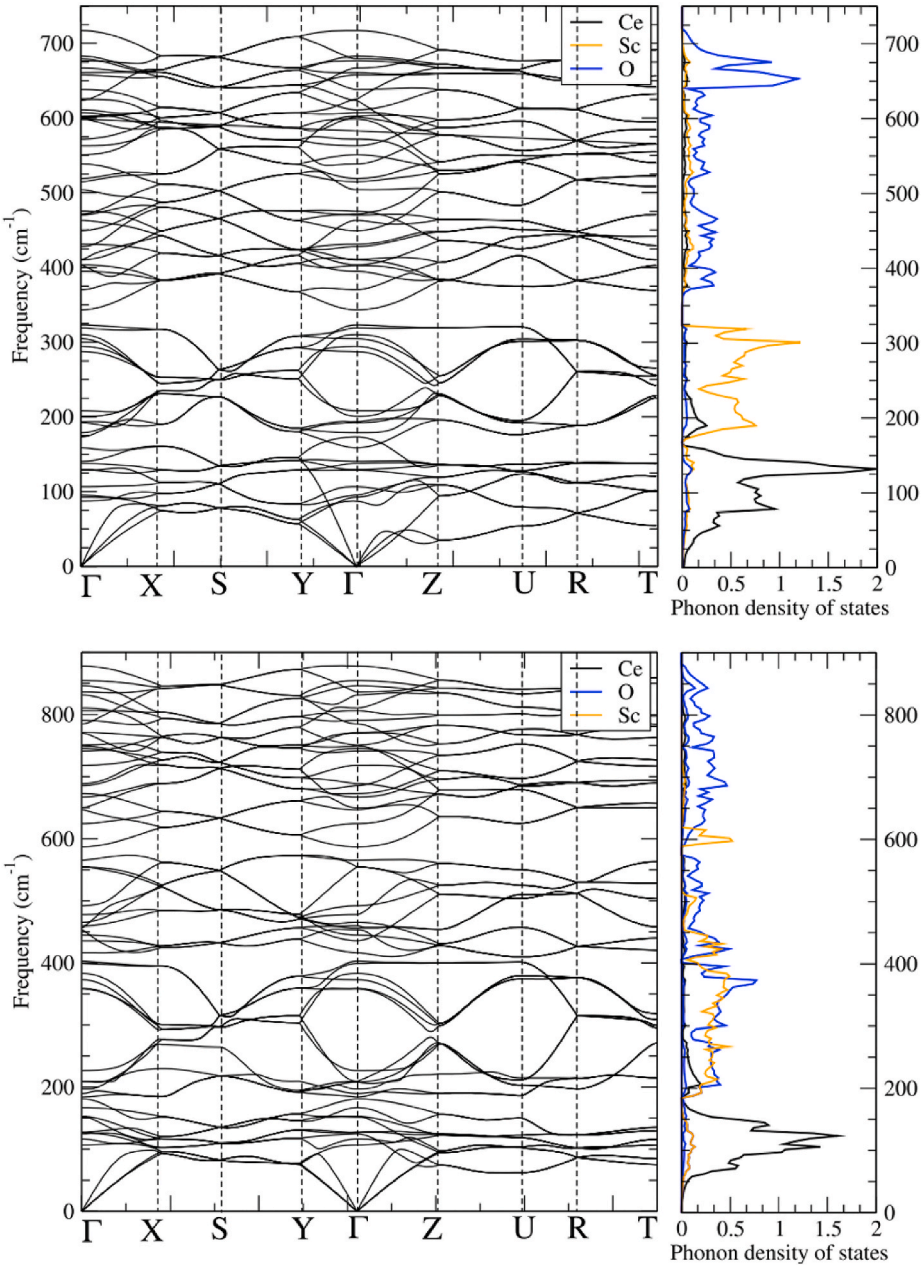

Fig. 6. Phonon dispersion and PDOS of $CeScO_3$, top at zero pressure and bottom at 40 Gpa.

2.2.2. Energy band structure and DOS analysis

The energy band structure clarifies the motion state of electrons in the crystal, and describes the energy with which electrons are forbidden or allowed, and the energy band structure of a material determines most of its optoelectronic properties [33,66,68–72]. The density of states (DOS) is essentially the number of different states that electrons are allowed to occupy at a specific energy level [31]. From the DOS map, such as bonding information, valence bandwidth, and conduction bandwidth, each orbital for the total state can be obtained. Therefore, the DOS can be said to be one of the most important concepts in DFT simulations.

Recently, Anurag Roy et al. explored the photothermal properties of halide-doped $MAPbI_{3-x}Br_x$ perovskites and used DFT simulations to calculate the band structures and DOS of $MAPbI_3$, $MAPbIBr_2$, and $MAPbBr_3$, respectively, as shown in Fig. 8a-c [48]. The band gaps calculated by DFT simulation are 1.61eV, 1.68eV, and 2.41eV, respectively. This result is consistent with what they observed from the diffuse reflectance spectra in Fig. 9, further confirming that the perovskite band gap widens with increasing Br content. This change in the band gap and crystal structure distortion suggests that the thermochromic properties of the material are increased after halide doping. At the same time, it also proves the accuracy of theoretical calculation. Recently, Pina pitriana et al. calculated the PDOS

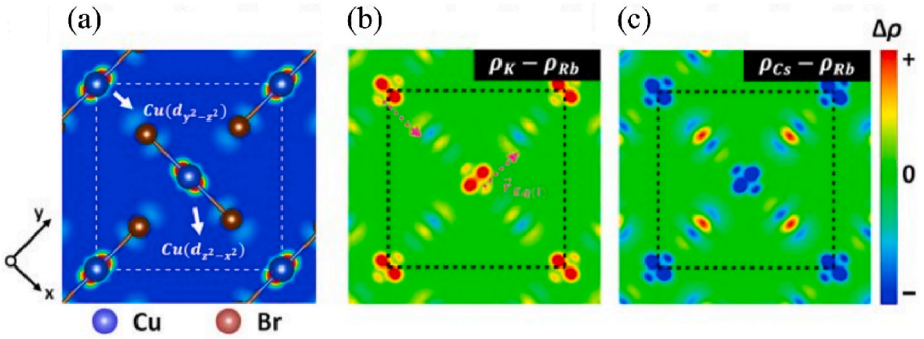

Fig. 7. (a) Spatial distribution of valence band maximum (VBM) state of Rb_2CuBr_4. The difference in the spatial distribution of VBM state between (b) K_2CuBr_4 and Rb_2CuBr_4 and (c) Cs_2CuBr_4 and Rb_2CuBr_4.

of $LiPbBr_3$, $NaPbBr_3$, $RbPbBr_3$, $KPbBr_3$ and $CsPbBr_3$ through DFT simulation to study the effect of A^+ cations on energy band characteristics [38]. As shown in Fig. 10a-e, the valence band (VB) shapes of the five perovskite minerals are very similar, and they are mainly composed of Br-4p orbitals. The conduction band (CB) is mainly composed of Pb-6p and A^+ cations orbitals. With the change of A^+ cations, their atomic orbitals fall below VB and their contribution to CB decreases, so only the Pb-6p orbitals mainly occupies CB at this time. This also proves that the A^+ cations has little influence on the band gap, and the change of the band gap mainly depends on the structure of $PbBr_6$.

2.3. Interface engineering

Interface engineering is to optimize perovskite materials through doping, substitution, and other means, to reduce interface defects, accelerate carrier transmission efficiency and change the phase transition stability of materials (Fig. 11). In addition to XRD, absorption spectroscopy and other means, we can also calculate the adsorption energy and defect formation energy of materials through DFT simulation to further understand the interface optimization process of perovskite [73–78].

2.3.1. Adsorption energy

The main research contents of adsorption kinetics are adsorption, desorption rate, and various influencing factors, which will help to further explore the mechanism of chemical adsorption and heterogeneous catalytic reaction [32,40,79–82]. Here, we use DFT to calculate the binding energies of amino, hydroxyl and oxygen double bonds on phenylalanine (PHE) with $MAPbI_3$ surface. As shown in Fig. 12a-c, the binding energy of the three binding modes are 5.12eV (NH_3-), 0.56eV (O =) and 5.47eV (OH-) respectively. The binding energy directly reflects the difficulty of the adsorption reaction, a lower binding energy represents a greater probability of the adsorption mode. Therefore, the O = adsorption mode is more likely to occur at the doping interface.

Recently, Cheng Chieh Lin et al. used the organic molecule hexamethyldisilane (HMS) as an additive to improve the stability of $CsPbI_3$ nanocrystals [83]. To determine the binding strength of polyethylene (OLA) and HMS with $CsPbI_3$ nanocrystals, they calculated the adsorption energy of the two ligands on the PbI_2 surface through DFT simulation, as shown in Fig. 13(a、b). The results show that the adsorption energy (−0.89 eV) of HMS on the surface of $CsPbI_3$ is much higher than that of OLA ligand (−0.37 eV). The stronger adsorption of HMS effectively stabilizes the perovskite phase and avoids the phase transition reaction. This phenomenon can be attributed to the sulfur atom of HMS as σ donor leads to stronger lewis base bonding on the surface of lead-rich perovskite, thus preventing the generation of surface defects.

2.3.2. Defect formation energy

Defect formation energy is an important index to measure the photoelectric properties of doped systems [31,64,84,85]. The formation of defects can directly reflect the difficulty of forming specific defects in materials, and its formula is as follows:

$$E_f = E_{dope} - E_{principal} - n_{dope}\mu_{dope} - n_{principal}\mu_{principal} \quad (4)$$

where E_f represents the defect formation energy, E_{dope} and $E_{principal}$ are the energies of the dopant and host, respectively, n represents the number, and μ represents the chemical potential of the corresponding atom, which can be calculated from the corresponding element.

According to DFT calculation, Yuan Cai et al. Selected the multifunctional molecule 2,2-difluoropropanediamide (DFPDA) to optimize the efficiency and performance of $FAPbI_3$ perovskite, achieving an efficiency of 22.21% and the stability of the device under wet, heat and light conditions [86]. Their passivation mechanism utilizes carbonyl, amino and fluoro functional groups on DFPDA. Amino groups can inhibit ion migration by binding with free iodine ions; the carbonyl group will fill the uncoordinated lead ions and reduce the crystallization rate; fluorine groups affect the hydrophobicity of perovskite, and they can improve the interlayer carrier

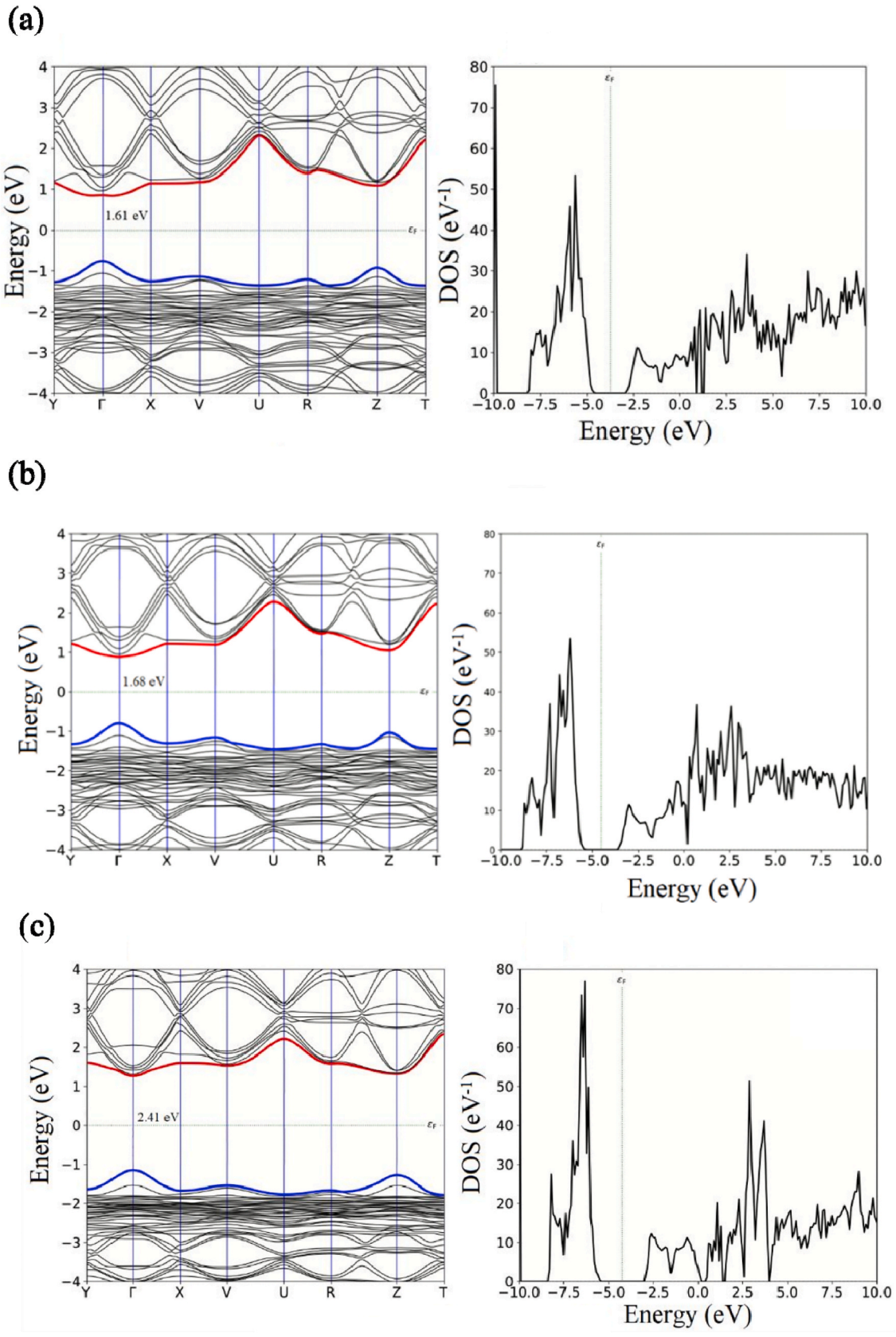

(caption on next page)

Fig. 8. Band structure and DOS of (a)$MAPbI_3$, (b)$MAPbIBr_2$ and (c)$MAPbBr_3$.

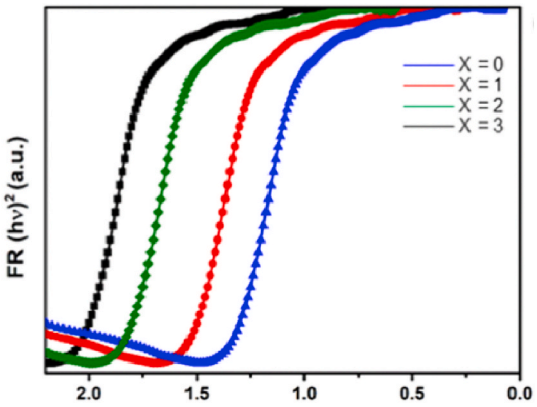

Fig. 9. Reflection spectrum of $MAPbI_3$, $MAPbIBr_2$ and $MAPbBr_3$.

transport between the transport layer and the functional layer. As shown in Fig. 14, after DFPDA treatment, the formation energy of iodine vacancies, lead vacancies and especially lead iodine inversion defects on the perovskite surface was significantly increased, indicating the inhibition ability of DFPDA on perovskite surface defects.

2.4. Thermoelectric properties

One of the important reasons of why perovskite has become a new type of smart window material is its excellent thermoelectric properties [87]. Perovskite thermoelectric materials have low thermal conductivity, and they have the characteristics of high carrier transport energy and high Seebeck coefficient. The thermoelectric efficiency of the material is generally characterized by the thermoelectric figure of merit (ZT). The calculation formula of ZT is as follows:

$$ZT = \frac{S^2 \sigma T}{k} \tag{5}$$

where S is the Seebeck coefficient, σ is the electrical conductivity, k is the thermal conductivity, and T is the absolute temperature. Materials with high thermoelectric efficiency require very low thermal conductivity as well as high electrical conductivity and thermal power (i.e., the absolute value of the Seebeck coefficient).

However, if the carrier concentration is simply increased, although the electrical conductivity can be increased, the thermal power may be reduced. Therefore, in order to obtain a higher thermoelectric figure of merit, it is necessary to find the dynamic balance of these three parameters.

Combining DFT simulations and Boltzmann transport theory, Lifu Yan et al. explored the carrier transport and thermoelectric properties of mixed halide perovskite $CsPb(I_{1-x}Br_x)_3$ doped with different concentrations of Br [88]. They first constructed 21 configurations with different concentrations of $CsPb(I_{1-x}br_x)_3$ along the x-axis, as shown in Fig. 15. In order to explore the relationship between carrier transport and thermoelectric characteristics, they constructed a function image of carrier concentration and Seebeck coefficient as shown in Fig. 16 (a) at a temperature of 300 K. As they expected, the carrier concentration is inversely proportional to the absolute value of the Seebeck coefficient. On the other hand, as shown in Fig. 17(a、b), the Seebeck coefficient shows a linear correlation with temperature in the range of 200 K–500 K. Next, they directly solved the Boltzmann transport equation to obtain the relationship between the relaxation time normalized conductivity and carrier concentration. As shown in Fig. 16b, the relaxation time normalized conductivity is positively correlated with the carrier concentration. They found that the reason for the remarkable ZT value of $CsPb(I_{1-x}Br_x)_3$ crystal form is its lower structural symmetry. The significant anisotropy of carrier transport caused by conduction band splitting results in low carrier effective mass (m*) (Fig. 18a) and transformational state constant (EDP) (Fig. 18b), resulting in high thermoelectric power factor. At the same time, the structural disorder of these hybrid perovskites leads to their ultra-low thermal conductivity. Therefore, these two factors simultaneously contribute to the excellent thermoelectric properties of the $CsPb(I_{1-x}Br_x)_3$ polymorph.

3. Perovskite thermochromic smart window

Perovskite materials have become the new candidate materials for the next generation of smart window devices because of their high carrier mobility, solvable preparation, adjustable band gap, and high low-temperature transmittance. At present, electrochromism and thermochromism are the mainstream color-changing mechanisms of smart windows. The electrochromic smart window is a reversible transition from the colored state to the faded state of the whole electrochromic device through the injection and

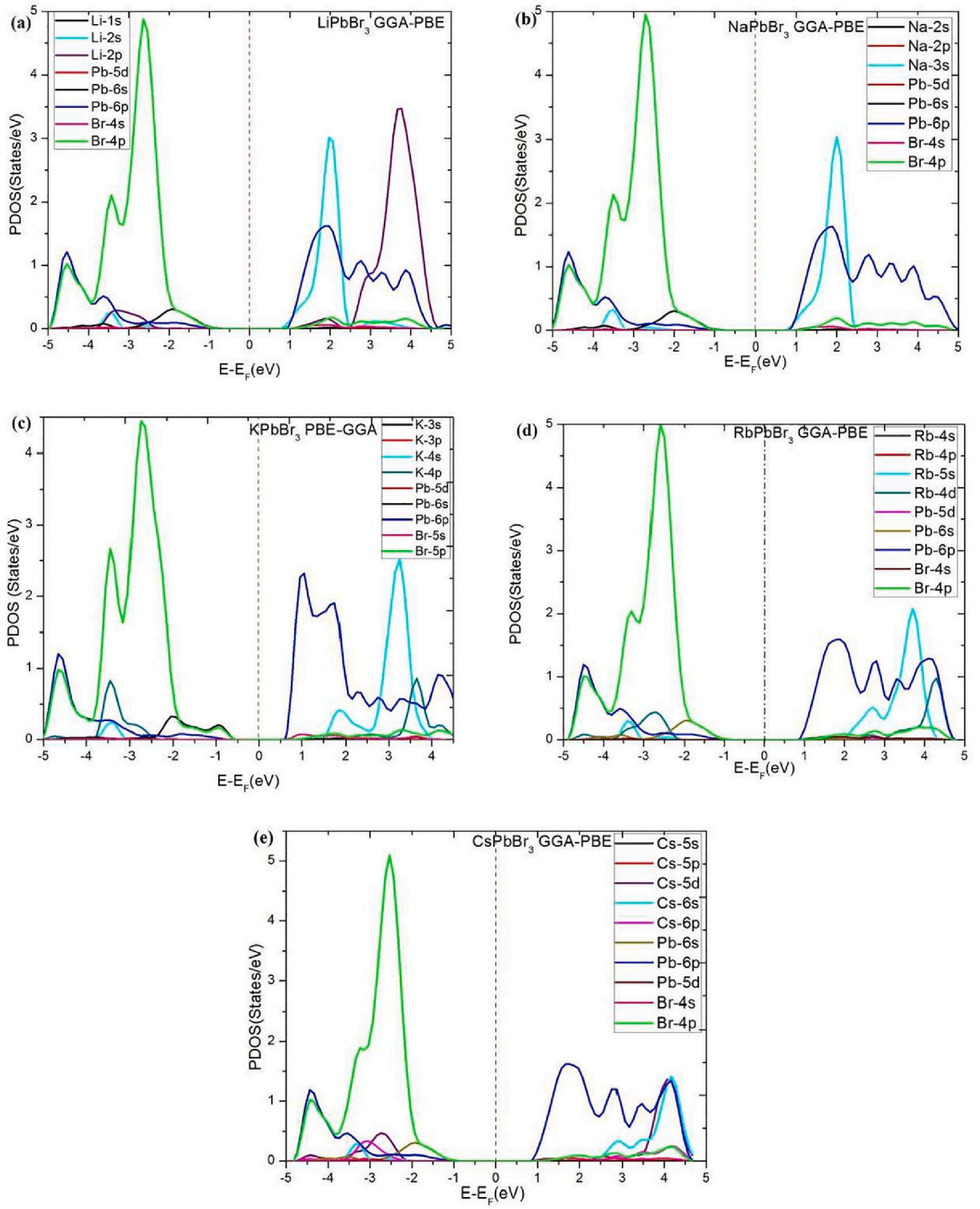

Fig. 10. Projected density of states (PDOS) of five kinds of cationic (a.Li、b. Na、c.Rb、d.K and e. Cs) perovskite.

extraction of ions in the electrochromic layer caused by the external electric field. Compared with electrochromism, thermochromism has the advantage that it does not require additional electrical stimulation, and only requires temperature changes to achieve the color change process. Perovskite materials are expected to reduce the transition temperature by doping substitution and other means. Once

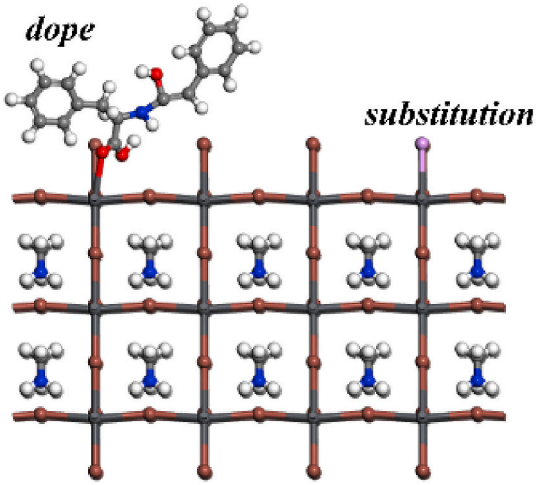

Fig. 11. DFT graphic simulation of passivation and doping of perovskite materials.

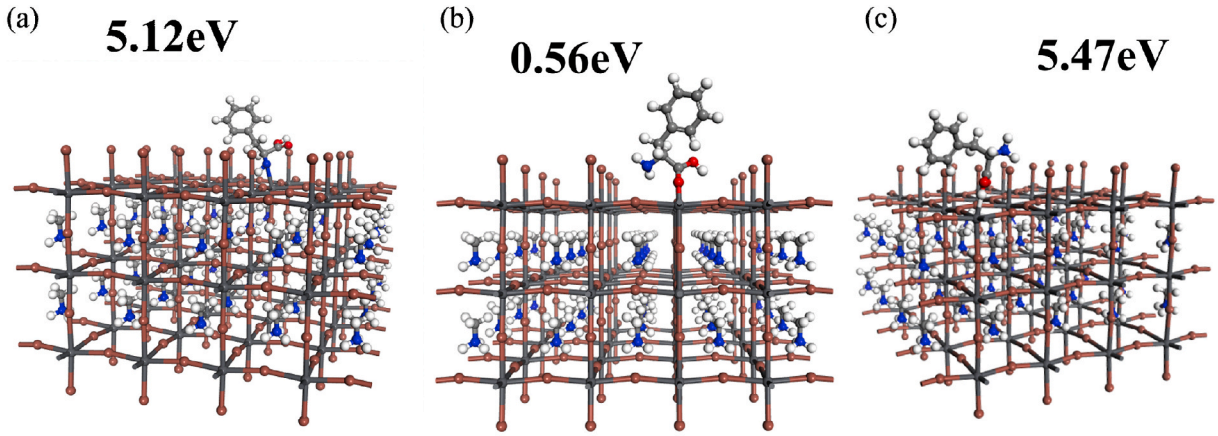

Fig. 12. (a)NH_3-, (b)O = , and(c)OH- adsorption models of PHE and $MAPbI_3$ surfaces and their binding energies.

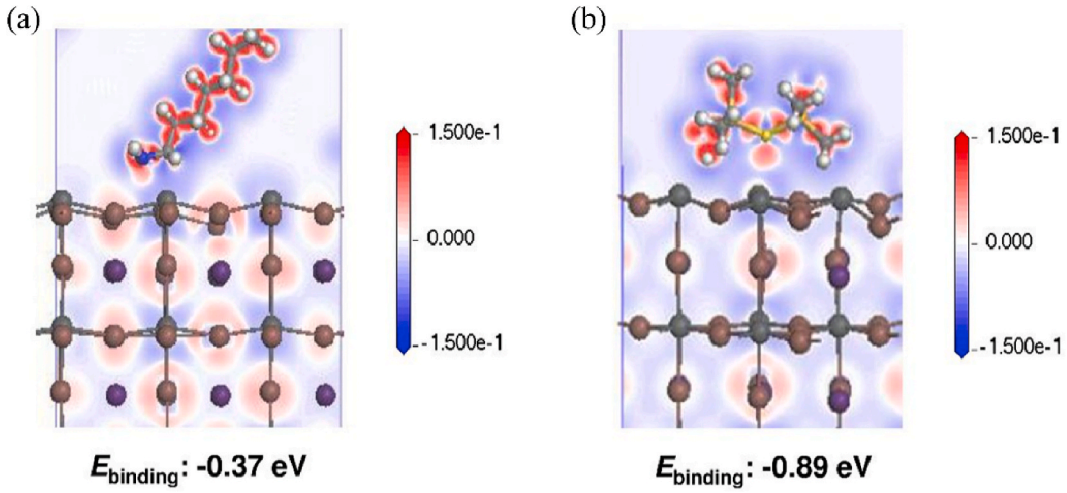

Fig. 13. DFT simulation of adsorption energy of(a)OLA and (b)HMS on PbI_2 surface.

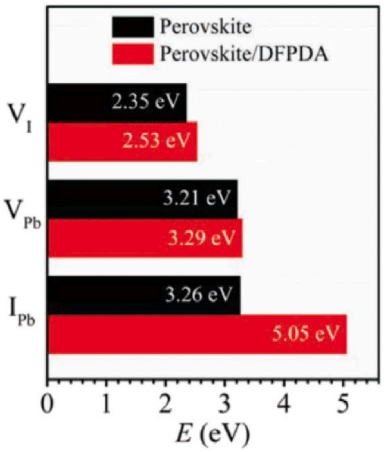

Fig. 14. Formation energy of three kinds of defects (I vacancy, Pb vacancy and I–Pb antisite) in perovskite before and after DFPDA passivation.

the transition temperature is reduced to room temperature, smart window devices can complete the self-adjusting color change process according to the changes of sunlight and ambient temperature. And smart window devices using perovskite materials can be used as solar cells while changing color, which will bring great help to energy engineering.

3.1. Thermochromic perovskite materials

The general structural formula of perovskite material is ABX_3, which originates from $CaTiO_3$ compound. After decades of development, perovskite has become the generic name of a series of compounds that conform to its general structural formula. The A site is usually occupied by cations with a larger ionic radius, while the cations occupying the B site (such as transition elements) usually have a smaller ionic radius. Its X position is occupied by anions, most of which are halogen elements. And different positions of perovskite can also be mixed by different elements in proportion, which makes perovskite materials very diverse. In the research of perovskite solar cells, the more common materials are $MAPbI_3$ ($CH_3NH_3PbI_3$), $CsPbBr_3$, etc. The main ways to improve efficiency are substitution, doping and low dimensional perovskite [48,57,58,62,75,89–94]. The structure of some perovskite materials will change its phase transition at a certain temperature so that the material band gap and material color will change. In recent years, a large number of related researches have been published, many of which have achieved good thermochromic effects by adjusting the proportion of X-site elements [35,63,83,95].

For example, the hydrated PTSW reported by Sai Liu et al., in 2020 realized the reversible transition from a transparent state to a dark brown red colored state by dissociating H_2O from $MAPbI_{3-x}Cl_x$ by heating and has a solar modulation efficiency of 23.7% [49]. In the experiment, they prepared MAI and $PbCl_2$ precursor solutions of different proportions, and prepared different perovskite samples by a spin coating method (Fig. 19a). They found that only the samples with a ratio of MAI and $PbCl_2$ higher than 6:1 can achieve reversible transformation. They measured the transmission spectra of perovskite thin films at low temperature and high temperature respectively (Fig. 19b). They found that the thermochromism of hydrated perovskite mainly regulates the visible light region (380–780 nm), but has no obvious effect on the infrared region (780–2500 nm). Although hydrated perovskite devices show good performance in the visible light range (solar energy modulation rate is 23.7%), most of the thermal radiation at room temperature comes from the infrared band, and their devices do not show very bright performance in this band, which, of course, indicates that how to broaden the absorption range is an urgent problem in the next development of perovskite smart windows. It is worth noting that they put hydrated perovskite samples in the environmental control room in the experiment, with the ambient temperature set at about 22 °C and the relative humidity adjusted between 30% and 10%. The results show that when the humidity decreases, the sample will gradually change from transparent to reddish brown, and when the humidity increases, the sample will also gradually fade from reddish brown to transparent. This shows that water vapor also plays a very important role in the reversible discoloration of hydrated perovskite. On the one hand, this result may prove the existence of a hydration mechanism from a practical point of view, but on the other hand, the impact of water vapor on hydrated perovskite also reminds us of a bottleneck in practical applications when hydrated perovskite smart window devices are used in extreme weather. In addition, in the process of preparing devices, it is necessary to strictly control the internal humidity of the controller to ensure the occurrence of a hydration reaction. Therefore, in addition to updating packaging technology, we still need to pay attention to the material itself and explore more spontaneous phase change structures. In addition, in this work, the average conversion temperature of the device is reduced to 40.1 °C. Compared with VO_2 materials, this is very excellent progress. However, this temperature is still higher than room temperature (≈25 °C), so we still need perovskite materials with a lower transition temperature.

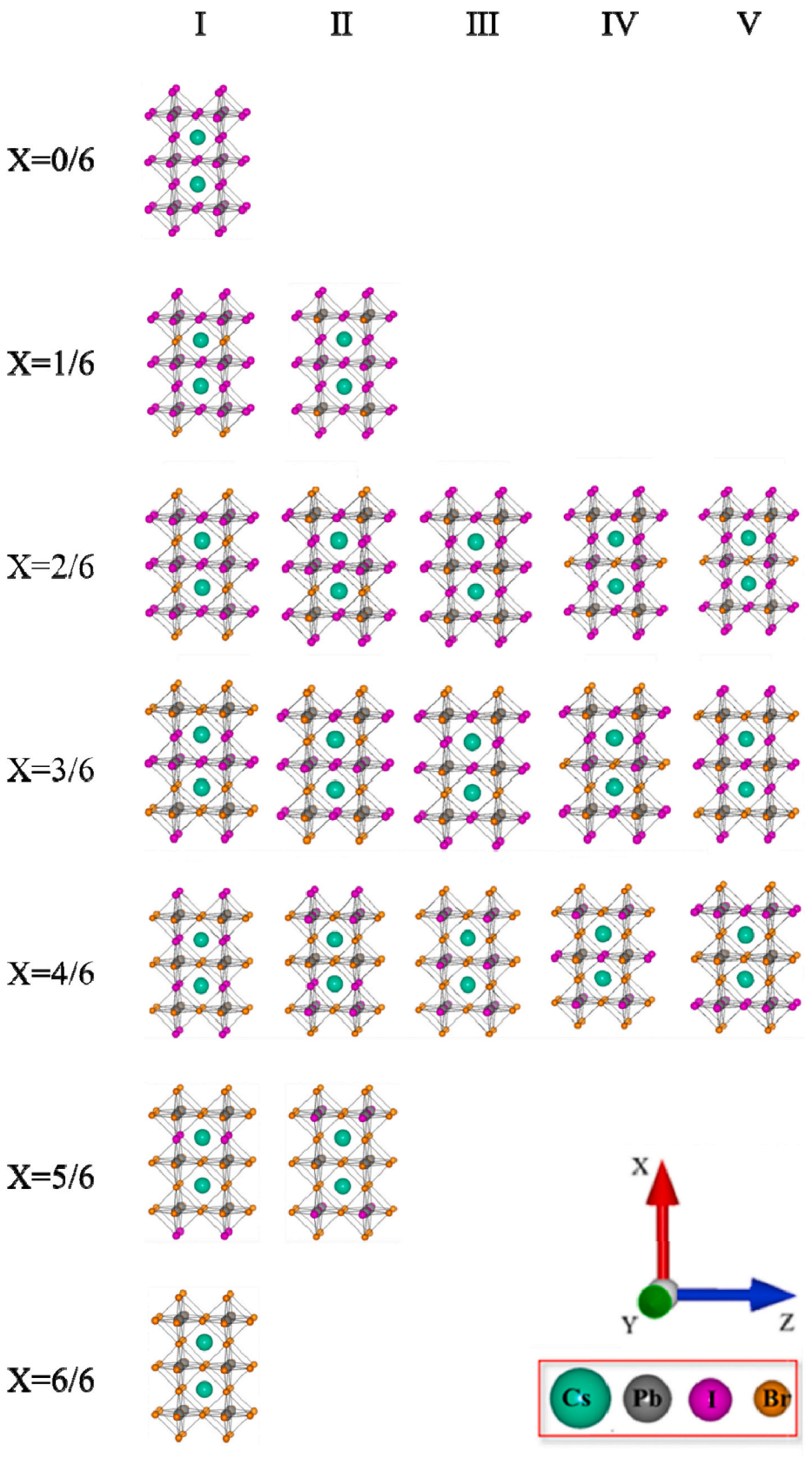

(caption on next page)

Fig. 15. 21 configurations of $CsPb(I_{1-x}Br_x)_3$ at different concentrations along the x-axis.

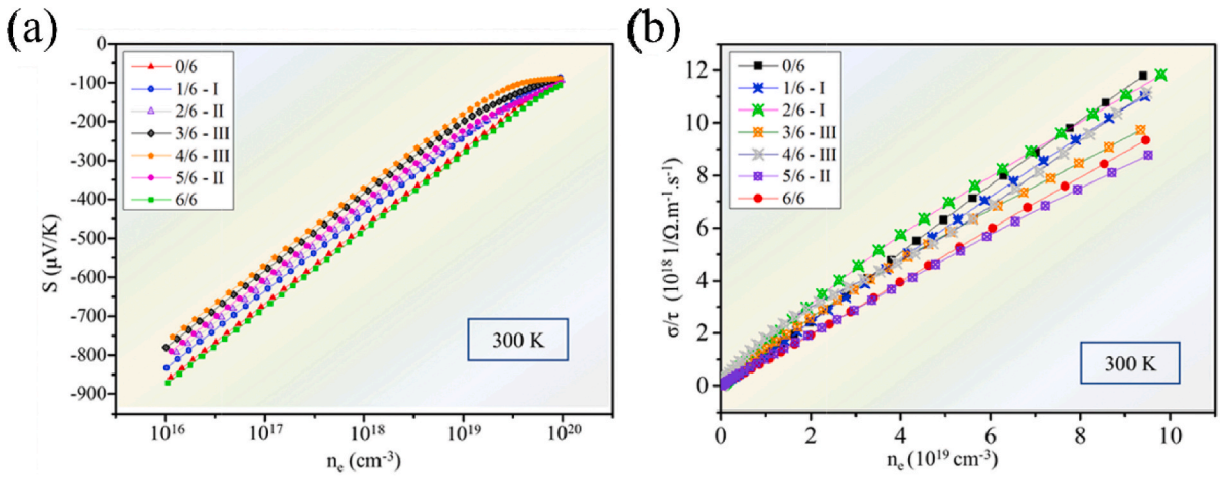

Fig. 16. (a) Function image of carrier concentration and Seebeck coefficient at 300 K (b) Relaxation time normalized conductivity and carrier concentration.

3.3. Absorption range

Because most of the heat radiation in the sunlight comes from the infrared region, it will cause a lot of energy waste in practical applications. In summer, a large amount of infrared radiation causes the room temperature to rise, which means that a large number of refrigeration systems are used; In winter, the room temperature decreases, but part of the infrared light entering the room will be consumed by reflection. Therefore, the smart window device can not only work in the visible light range, it should also have a certain blocking and modulation ability for infrared light. However, most perovskite materials do not work well in the NIR range, so how to improve their NIR modulation ability has become a popular research direction [44,96–99].

To solve the above problems, Sai Liu et al. reported a further study in 2021. They proposed a strategy of integrating perovskite with high NIR absorption performance photothermal materials and low emission (low-E) layers [50]. As shown in Fig. 20, they prepared a thermochromic perovskite material (T-Perovskite) using a precursor with an MAI and $PbCl_2$ ratio of 6.5:1. The NIR absorption material selected cesium-doped tungsten trioxide (CWO), while the Low-E material used a SnO_2–Ag–SnO_2 structure with high visible light transparency (≈85%). This smart window uses the photothermal properties of CWO to adjust the temperature of T-perovskite to trigger its phase change and color change process. When the NIR radiation is low, CWO cannot heat the T-perovskite to the phase transition temperature, and the device maintains high transmittance to ensure the indoor brightness. With the enhancement of NIR radiation, T-perovskite reaches the phase transition temperature, and the device quickly changes color to block the visible light and NIR radiation, and significantly reduce the indoor temperature rise caused by sunlight. In addition, the low-E layer not only protects the indoor environment from the impact of high temperature of windows, but also reduces the radiation heat loss of smart windows. A moderate transition temperature (T_c) is very important for a thermochromic smart window. To determine the Tc of the laminated smart window device and whether the low-E layer will affect the transition temperature of T-perovskite, they calculated the T_c of the smart window with (T-PCL) and without (T-PC) low-E layer respectively (Fig. 21). The results show that the conversion process of the two windows is almost the same, T_c of T-PC smart window in hot state and cold state is 42.6 °C and 36.1 °C respectively, while the T_c of T-PCL smart window is 42.4 °C and 35.3 °C respectively, which proves that Low-E coating does not affect T_c of T-Perovskite. The T-PCL window using this strategy can achieve adaptive adjustment of sunlight in multiple spectral regions and has a reversible transmittance change of 65.7%–25.6%. The NIR absorption reaches 78.2% and the radiation is less than 0.3. They also conducted field tests of model houses in Hong Kong's subtropical climate to evaluate the performance of T-PCL in practical applications (Fig. 22). They used acrylic boxes to make four sizes of 20 × 20 × 20 cm^3 model house, and seal it with thermal insulation material (Fig. 22a). They used thermocouples to monitor the indoor temperature and installed four types of windows (9 × 9 cm^2) on four model houses: ordinary window is used on model house 1 (MH_1), Low-E window is used on MH_2, T-PC window is used on MH_3, and T-PCL window is used on MH_4 (Fig. 22b). The physical model is shown in Fig. 22c. When the solar radiation reaches its peak at noon, the surface temperature of each window photographed by the infrared camera is about 900Wm^{-2}. At this time, the temperature of the four windows is as shown in Fig. 22d. The window temperature of MH_1 and MH_2 only reaches 35.5 and 38.0 °C, which is lower than the thermal state transition temperature of perovskite. In contrast, the window temperature of MH_3 and MH_4 reach 56.0 and 58.3 °C, respectively, which is sufficient to activate the thermochromic effect. Fig. 22e shows the indoor temperature curves of the four model houses. During the day, the indoor temperature of MH_1 was the highest, reaching a peak of 47.7 °C at about 14:00. Compared with MH_1, the peak temperature of MH_2 decreased by 1.5 °C, and the indoor peak temperatures of MH_3 and MH_4 are 40.7 and 39.7 °C respectively, 7.0 and 8.0 °C lower than MH_1. They also recorded the whole reversible thermochromic process of T-PCL window as shown in Fig. 22f. This work shows the

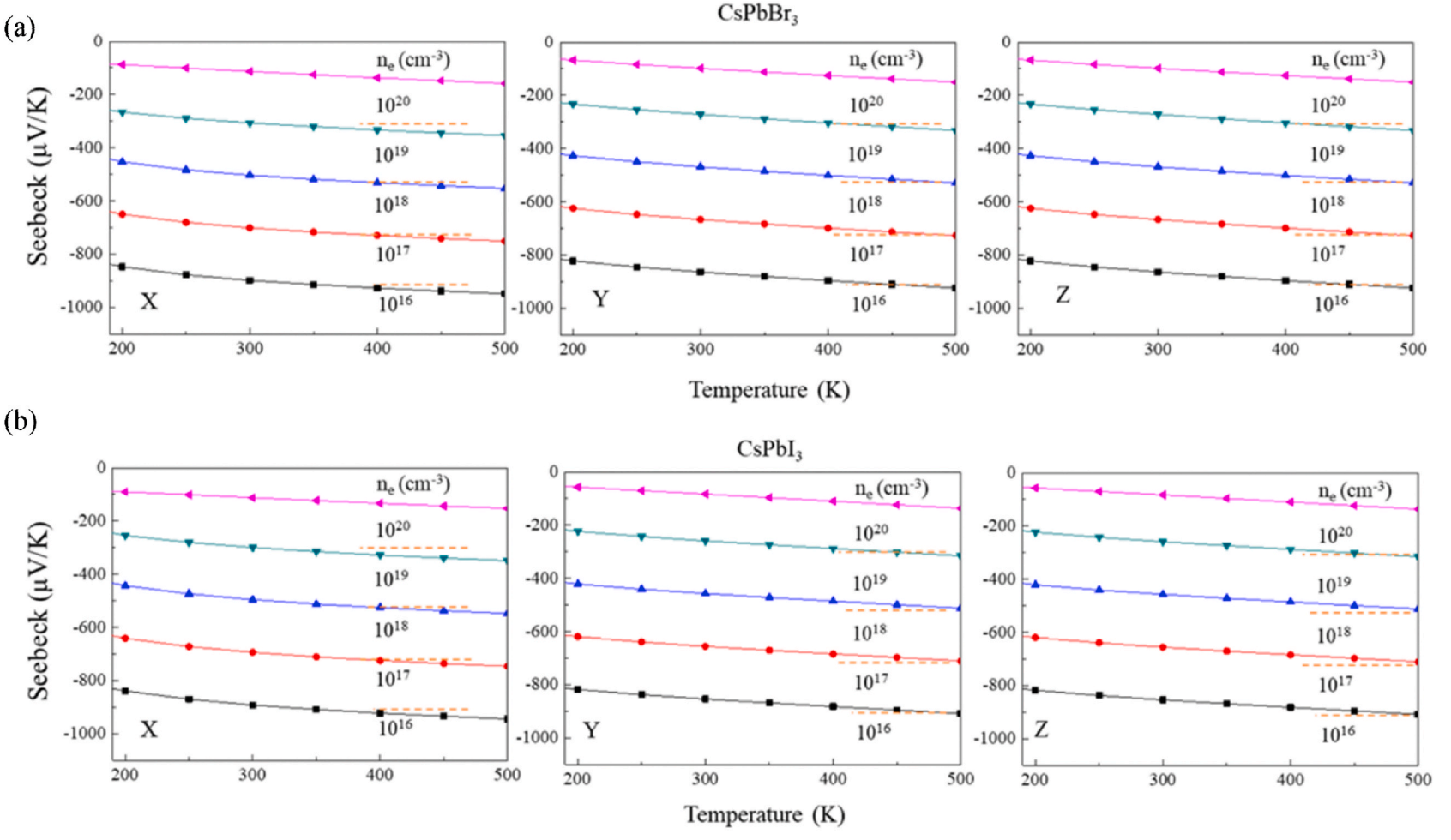

Fig. 17. Linear relationship between Seebeck coefficient and temperature.

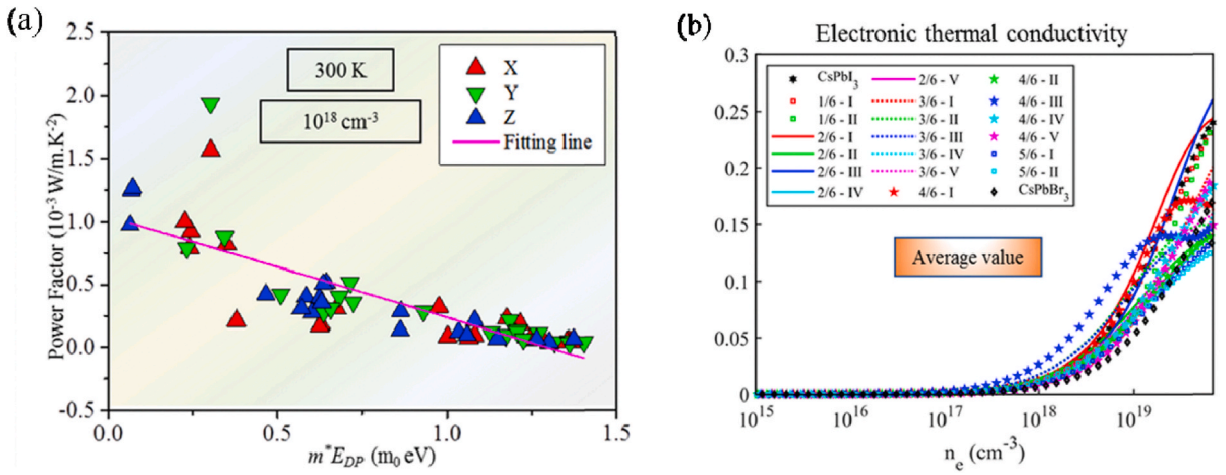

Fig. 18. (a) Carrier effective mass (m*) and variable potential constant (EDP) of mixed perovskite (b) Thermoelectric power factor of mixed perovskite.

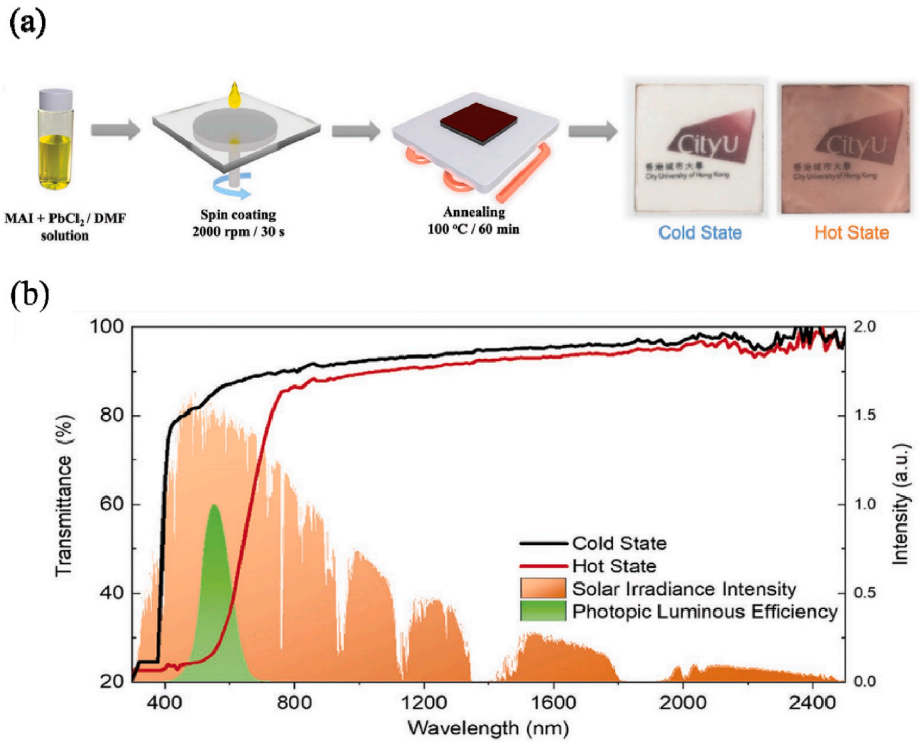

Fig. 19. (a) Device preparation process and low/high temperature physical diagram of the device (b) Transmission spectra of perovskite thin films at low and high temperatures.

great development potential of the integrated perovskite intelligent window and shows the remarkable energy-saving effect. It also shows that the performance display of the intelligent window devices must be combined with the actual conditions. For example, the on-site test of the model house they showed provided us with a good solution. However, the size of windows in life is much larger than the size of model windows. The spin coating method they used to make T-PSL windows in the model will be extremely difficult to make large-area devices. Therefore, how to change the preparation process to make smart window devices larger is still a problem that we need to solve. Similarly, a large area will also bring great challenges to the film quality and stability of perovskite materials. In addition, with the rise of DFT simulation in the field of materials science, should we also try to apply DFT simulation to the field of smart windows?

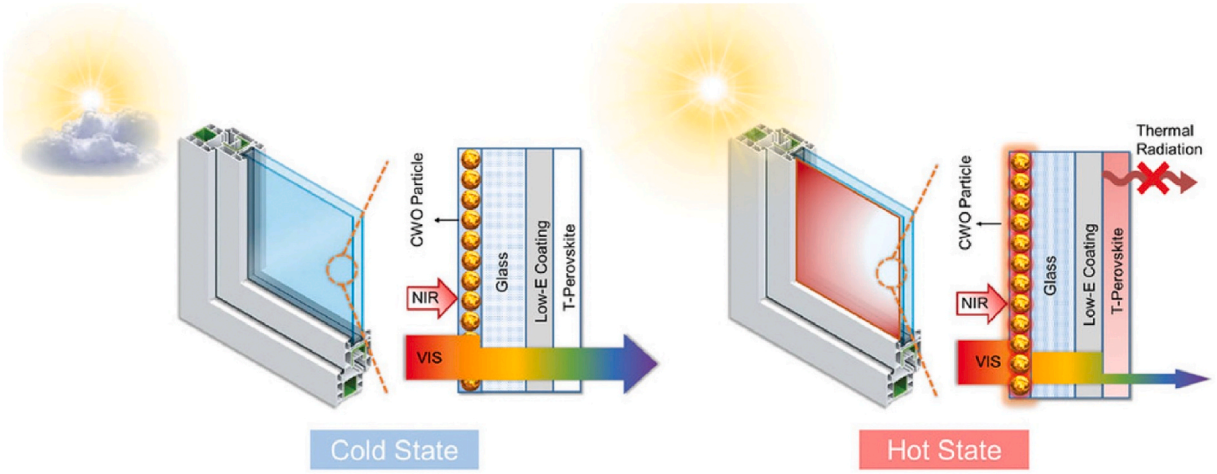

Fig. 20. The structure and the working principle of the Perovskite/CWO/low-E smart window.

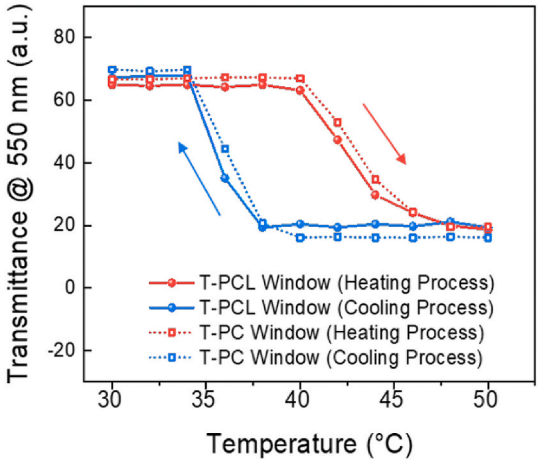

Fig. 21. Transmittance (550 nm) of T-PC window and T-PCL window during heating and cooling processes.

3.3. DFT application

DFT simulation has been widely used in the field of materials science [31,32,34,39,40,66,68,69,72,73,79–82,84,85,100]. It shows considerable accuracy in energy calculation and energy band analysis. And in the field of perovskite solar cells, it has been widely used to calculate defects, which has saved a lot of material costs for the experimental process. Similarly, we can also apply DFT to the material analysis of smart windows.

For example, Anurag Roy and others provided us with a successful case of DFT simulation in the field of smart windows. In 2021, they discussed the modulation of Br doping on the photothermal properties of mixed halide hybrid perovskite $CH_3NH_3PbI_3$ through experiments and DFT simulation [48]. They found that $CH_3NH_3PbIBr_2$ material has a semi-reversible color change behavior from yellow (22 °C) to maroon (60 °C), and has a transition temperature close to room temperature (40 °C). In addition to what is shown in Fig. 8 above, they used DFT simulation to calculate the band gap of different proportions of Br-doped $MAPbI_3$ materials. To reveal the interaction mechanism between water molecules and perovskite materials, they also calculated the interaction between water molecules and $MAPbIBr_2$ surface. First, they modeled the tetragonal unit cell of $MAPbI_3$ using the 14/mcm space group and lattice parameters a = b = 8.4822 Å and c = 11.9944 Å, and then expand to 2 × 2 × 2 supercells. Similarly, they established the models of $MAPbIBr_2$ and $MAPbBr_3$. Then, they cut out the corresponding surfaces of the three materials along the [0 0 1] direction. The structure optimized by DFT relative relaxation is visualized by VNL version 2019.12 software (as shown in Fig. 23 a, b, c). The structure after hydration (Fig. 23 d, e, f) can observe a significant reduction in lattice distortion, and the energy band structure and DOS calculated by DFT simulation show that the band gap of $MAPbIBr_2$ after hydration decreases from 2.17eV to 2.02eV. They demonstrated through simulation that water can improve the thermochromic properties of perovskite materials. In addition, according to their adsorption energy formula, the interaction energy between water and $MAPbI_3$, $MAPbIBr_2$ and $MAPbBr_3$ is 0.50 eV, 0.06 eV and 0.33 eV, respectively. This result shows that $MAPbIBr_2$ has a strong desire for water molecules in terms of interaction. This work is a successful

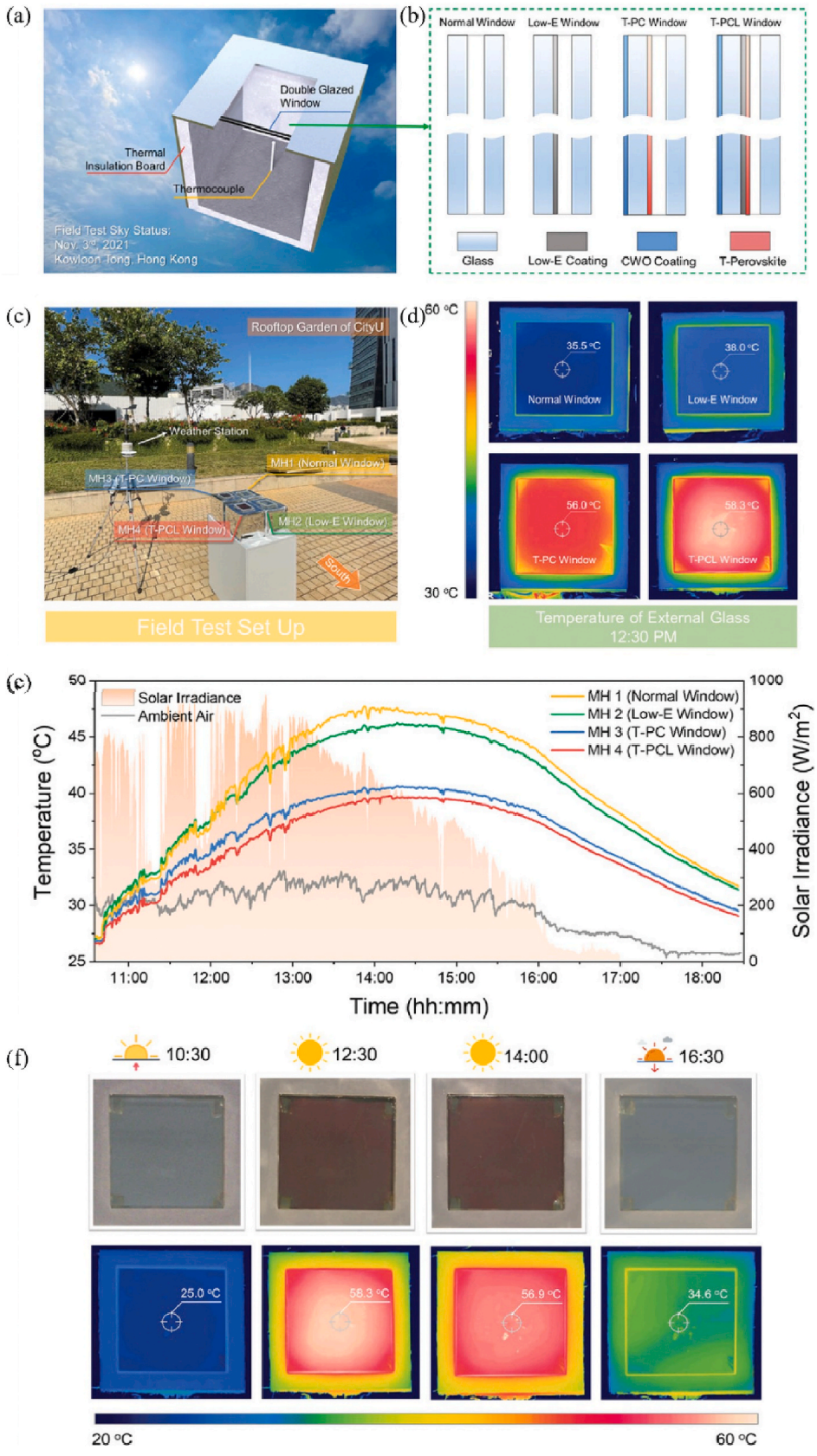

(caption on next page)

Fig. 22. Field test of model room. (a) Composition of the model room. (b) Four kinds of windows for model room. (c) Experimental device for field test of model room. (d) Surface temperature of four kinds of windows at noon. (e) Indoor temperature curve for field test of model house on November 3, 2021 in Hong Kong.(f) Test the real objects and infrared images of the T-PCL smart window on that day.

attempt to combine experimental and theoretical calculation methods. They fully demonstrated the advantages of theoretical calculation in reaction mechanisms and other aspects. In addition, the theoretical calculation still has huge potential to be explored in the prediction of thermochromic materials. In addition, although their work shows a good transition temperature, the device's incomplete reversibility still limits its practical application, which is also the key to continuous exploration and research in the next step.

Also, for example, Armin Sahinovic and Benjamin Geisler successfully predicted the properties of perovskite materials that can be composed of all elements in the periodic table by combining the deep learning of artificial neural networks (NNs) with DFT simulation, and the accuracy was completely within the error range of DFT simulation calculation itself [101]. This also provides new ideas for our next work. We can try to build a complete material prediction system, similar to the combination of neural network and DFT simulation, which will greatly reduce the economic cost and time cost of the experiment.

4. Summary and outlook

In conclusion, we summarized the application of DFT calculation in thermochromic perovskite smart windows. We review and discuss the related work of DFT calculation, from crystal, electronic structure characteristics, and interface engineering to thermoelectric characteristics. These works prove that DFT simulation can be perfectly applied to the thermochromic perovskite intelligent window by simulating and analyzing the thermal-induced phase transition, the stability of the electronic structure, the energy band

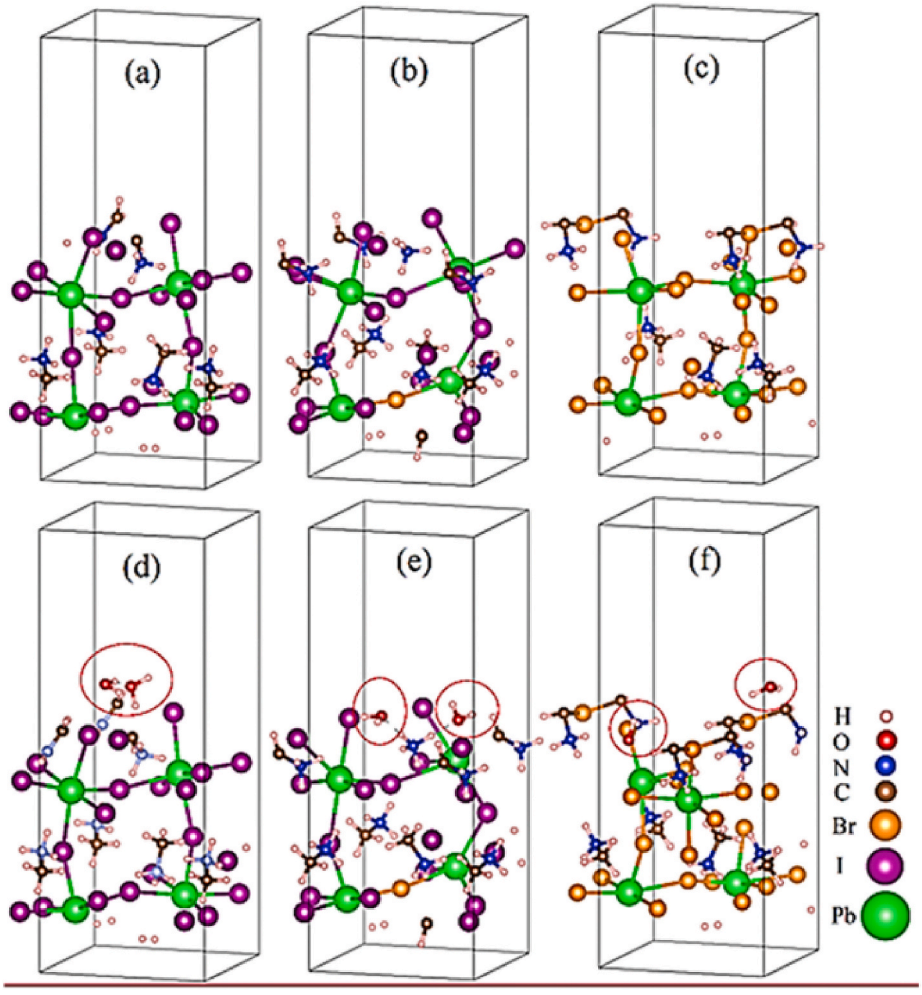

Fig. 23. Optimized relaxed geometry of (a) $MAPbI_3$(0 0 1), (b) $MAPbIBr_2$(0 0 1), (c) $MAPbBr_3$(0 0 1), (d) $MAPbI_3$(0 0 1)@H_2O, (e) $MAPbIBr_2$(0 0 1) @H_2O, and (f) $MAPbBr_3$(0 0 1)@ H_2O.

structure, and the density of states. The calculation of adsorption energy and thermoelectric quality factor provides a deeper exploration of the interface and thermoelectric properties of materials. Then, we reviewed the recent progress of thermochromic perovskite smart windows from three aspects: perovskite thermochromic materials, absorption range, and DFT applications. Perovskite shows a very excellent development prospect as a thermochromic material, and the application of DFT simulation in smart windows is expected to make an initial great contribution to saving experimental costs and material prediction.

In the aspect of perovskite thermochromism, although there has been good progress in the performance of devices such as transition temperature, we still need to make great efforts to put PTSW devices into real life. First of all, we need to try to apply large-area preparation processes such as scratch coating, ink-jet printing and vapor deposition to the field of PTSW, and still need to invest a lot of energy in the work related to defect passivation and stability improvement of perovskite materials. Because the large area of devices will make perovskite materials more prone to defects, and in practical applications, extreme weather and longer working hours will put forward higher requirements on the durability of devices (light, humidity, heat). In addition, from the perspective of saving experimental costs and revealing the discoloration mechanism, we should apply DFT simulation to the field of smart windows. DFT simulation has shown excellent accuracy in predicting material structure and optical properties, and also provides a high degree of freedom in structural modeling. In addition, in the industrialization process of smart windows, environmental protection has always been a very important issue. At present, the functional layer materials used in most perovskite thermochromic smart window devices is lead-based perovskite, which will bring great risks to the recovery and degradation in practical applications. Therefore, while improving the device's performance, we should try to apply lead-free perovskite materials in the field of smart windows. Given the extensive application of perovskite materials in solar cells, organic displays and other fields, we should try to integrate multiple functions in perovskite smart window devices. We believe that in the next stage, the smart window will be developed into a new generation of energy-saving devices that integrate functions such as self-regulating color change, power supply, and display, and it is not impossible to realize multiple functions with one material as the main body.

Acknowledgments

This study was supported by the National Natural Science Foundation of China (Grant Nos. 61974054 and 61675088), the International Science & Technology Cooperation Program of Jilin (Grant No. 20190701023GH), the Scientific and Technological Developing Scheme of Jilin Province (Grant No. 20200401045GX), and the Project of Science and Technology Development Plan of Jilin Province (Grant No. 20190302011G).

References

[1] Energy outlook 2022. https://www.bp.com/en/global/corporate/energy-economics/energy-outlook.html, 2022.
[2] F. ISE, PHOTOVOLTAICS REPORT, Fraunhofer ISE, 2022. https://www.ise.fraunhofer.de/de/veroeffentlichungen/studien/photovoltaics-report.html.
[3] S. Wang, W. Gao, X.Y. Hu, Y.Z. Shen, L. Wang, Chem. Commun. 55 (29) (2019) 4137–4149.
[4] R. Yin, P. Xu, P. Shen, Energy Build. 45 (2012) 132–140.
[5] S.C. Sugarman, HVAC Fundamentals, River Publishers, 2020.
[6] S.J. Lee, D.S. Choi, S.H. Kang, W.S. Yang, S. Nahm, S.H. Han, T. Kim, ACS Sustain. Chem. Eng. 7 (7) (2019) 7111–7117.
[7] J.L. Wang, S.Z. Sheng, Z. He, R. Wang, Z. Pan, H.Y. Zhao, J.W. Liu, S.H. Yu, Nano Lett. 21 (23) (2021) 9976–9982.
[8] Q. Zhao, J. Wang, Y. Cui, X. Ai, Z. Chen, C. Cao, F. Xu, Y. Gao, Mater. Adv. 2 (14) (2021) 4667–4676.
[9] R. Zheng, Y. Wang, J. Pan, H.A. Malik, H. Zhang, C. Jia, X. Weng, J. Xie, L. Deng, ACS Appl. Mater. Interfaces 12 (24) (2020) 27526–27536.
[10] C. Meng, M.C. Tseng, S.T. Tang, C.X. Zhao, S.Y. Yeung, H.S. Kwok, Liq. Cryst. 46 (3) (2018) 484–491.
[11] J. Wang, C. Meng, C.-T. Wang, C.-H. Liu, Y.-H. Chang, C.-C. Li, H.-Y. Tseng, H.-S. Kwok, Y. Zi, Nano Energy 85 (2021).
[12] J. Li, X. Lu, Y. Zhang, X. Ke, X. Wen, F. Cheng, C. Wei, Y. Li, K. Yao, S. Yang, Adv. Funct. Mater. 31 (32) (2021).
[13] P. Si, L. Yu, B. Zhao, ACS Appl. Mater. Interfaces 12 (24) (2020) 27607–27613.
[14] C. Meng, M. Tseng, S. Tang, C. Zhao, F. Yeung, C. Coughlan, H.-S. Kwok, IEEE Photon. Technol. Lett. 30 (22) (2018) 1964–1967.
[15] Y. Ke, J. Chen, G. Lin, S. Wang, Y. Zhou, J. Yin, P.S. Lee, Y. Long, Adv. Energy Mater. 9 (39) (2019).
[16] Y. Zhou, X. Dong, Y. Mi, F. Fan, Q. Xu, H. Zhao, S. Wang, Y. Long, J. Mater. Chem. 8 (20) (2020) 10007–10025.
[17] S. Liu, C.Y. Tso, H.H. Lee, Y.W. Du, K.M. Yu, S.P. Feng, B. Huang, ACS Appl. Mater. Interfaces 13 (19) (2021) 22495–22504.
[18] Y. Cui, Y. Ke, C. Liu, Z. Chen, N. Wang, L. Zhang, Y. Zhou, S. Wang, Y. Gao, Y. Long, Joule 2 (9) (2018) 1707–1746.
[19] S. Liu, C.Y. Tso, H.H. Lee, Y. Zhang, K.M. Yu, C.Y.H. Chao, Sci. Rep. 10 (1) (2020), 11376.
[20] J. Kim, T. Paik, Nanomaterials 11 (10) (2021) 2674.
[21] J. Sang, W. Zhu, Y. Feng, Y. Liu, J. Shang, J. Sun, L. Guo, Y. Zhang, S. Zhao, V. Chigrinov, ACS Appl. Electr. Mater. 3 (11) (2021) 4882–4890.
[22] Z. Zhao, Y. Liu, D. Wang, C. Ling, Q. Chang, J. Li, Y. Zhao, H. Jin, Sol. Energy Mater. Sol. Cell. 209 (2020), 110443.
[23] L. Zhang, H. Xia, F. Xia, Y. Du, Y. Wu, Y. Gao, ACS Appl. Energy Mater. 4 (9) (2021) 9783–9791.
[24] L. Tang, L. Wang, X. Yang, Y. Feng, Y. Li, W. Feng, Prog. Mater. Sci. 115 (2021), 100702.
[25] Y. Ding, Y. Yan, Q. Peng, B. Wang, Y. Xing, Z. Hua, Z. Wang, ACS Appl. Poly. Mater. 2 (8) (2020) 3259–3266.
[26] X.-H. Li, C. Liu, S.-P. Feng, N.X. Fang, Joule 3 (1) (2019) 290–302.
[27] M. Guo, Q. Yu, X. Wang, W. Xu, Y. Wei, Y. Ma, J. Yu, B. Ding, ACS Appl. Mater. Interfaces 13 (4) (2021) 5634–5644.
[28] K. Li, S. Meng, S. Xia, X. Ren, G. Gao, ACS Appl. Mater. Interfaces 12 (37) (2020) 42193–42201.
[29] J. Lin, M. Lai, L. Dou, C.S. Kley, H. Chen, F. Peng, J. Sun, D. Lu, S.A. Hawks, C. Xie, F. Cui, A.P. Alivisatos, D.T. Limmer, P. Yang, Nat. Mater. 17 (3) (2018) 261–267.
[30] Y. Zhang, C. Tso, J.S. Iñigo, S. Liu, H. Miyazaki, C.Y. Chao, K.M. Yu, Appl. Energy 254 (2019), 113690.
[31] M.G. Ahangari, A.H. Mashhadzadeh, M. Fathalian, A. Dadrasi, Y. Rostamiyan, A. Mallahi, Vacuum 165 (2019) 26–34.
[32] F. Bakhshi, N. Farhadian, Int. J. Hydrogen Energy 43 (17) (2018) 8355–8364.
[33] M. Caid, H. Rached, A. Bentouaf, D. Rached, Y. Rached, Comput. Condens. Matter 29 (2021), e00598.
[34] E.D. Farias, M.E.Z. Michoff, V.S. Occello, V. Brunetti, M.C. Passeggi, T. Glatzel, Appl. Surf. Sci. 565 (2021), 150552.
[35] T. Ghrib, A. Rached, E. Algrafy, I.A. Al-nauim, H. Albalawi, M. Ashiq, B.U. Haq, Q. Mahmood, Mater. Chem. Phys. 264 (2021), 124435.
[36] M.M. Hasan, A. Kumer, U. Chakma, Adv. J. Chem.-Sec. A 3 (5) (2020) 639–644.
[37] T.G. Liashenko, E.D. Cherotchenko, A.P. Pushkarev, V. Pakstas, A. Naujokaitis, S.A. Khubezhov, R.G. Polozkov, K.B. Agapev, A.A. Zakhidov, I.A. Shelykh, S. V. Makarov, Phys. Chem. Chem. Phys. 21 (35) (2019) 18930–18938.

[38] P. Pitriana, T.D.K. Wungu, Herman, R. Hidayat, Results Phys. 15 (2019).
[39] T.V. Vu, I. Luzhnyi, G. Myronchuk, V. Bekenev, M. Bohdanyuk, A. Lavrentyev, B. Gabrelian, O. Parasyuk, O. Khyzhun, Opt. Mater. 114 (2021), 110982.
[40] G. Yan, Z. Gao, M. Zhao, W. Yang, X. Ding, Fuel 282 (2020), 118781.
[41] S. Tan, I. Yavuz, N. De Marco, T. Huang, S.J. Lee, C.S. Choi, M. Wang, S. Nuryyeva, R. Wang, Y. Zhao, H.C. Wang, T.H. Han, B. Dunn, Y. Huang, J.W. Lee, Y. Yang, Adv. Mater. 32 (11) (2020), e1906995.
[42] H. Zong, D. Zhou, L. Yan, H. Liu, J. Wu, Q. Hu, C. Kang, M. Li, Appl. Phys. A 127 (6) (2021).
[43] Z. Fang, S. Tian, B. Li, Q. Liu, B. Liu, X. Zhao, G. Sankar, Appl. Surf. Sci. 540 (2021), 148414.
[44] Z. Wang, B. Li, S. Tian, B. Liu, X. Zhao, X. Zhou, G. Tang, A. Pang, Materials 14 (17) (2021).
[45] J.B. Kim, D. Lee, I.H. Yeo, H.Y. Woo, D.W. Kim, J.-Y. Chae, D.W. Lee, S.H. Han, T. Paik, Solar Energy Materials and Solar Cells **226**, 2021.
[46] J. Tian, H. Peng, X. Du, H. Wang, X. Cheng, Z. Du, J. Alloys Compd. 858 (2021).
[47] Y. Feng, M. Yang, Y. Zhang, H. Liu, H. Ju, G. Zhang, W. Ma, Y. Wu, Y. Yu, Y. Yang, D. Liu, J. Chem. Sci. 134 (1) (2022) 24.
[48] A. Roy, H. Ullah, A. Ghosh, H. Baig, S. Sundaram, A.A. Tahir, T.K. Mallick, J. Phys. Chem. C 125 (32) (2021) 18058–18070.
[49] S. Liu, Y.W. Du, C.Y. Tso, H.H. Lee, R. Cheng, S.P. Feng, K.M. Yu, Adv. Funct. Mater. 31 (26) (2021), 2010426.
[50] S. Liu, Y. Li, Y. Wang, K.M. Yu, B. Huang, C.Y. Tso, Adv. Sci. 9 (14) (2022), e2106090.
[51] Q. He, B. Yu, Z. Li, Y. Zhao, Energy Environ. Mater. 2 (4) (2019) 264–279.
[52] Z. Li, S. Zhao, Z. Shao, H. Jia, A. Huang, P. Jin, X. Cao, Chem. Eng. J. (2022), 137556.
[53] H. Zhu, Z. Zhang, X. Jiang, J. Nanosci. Nanotechnol. 20 (3) (2020) 1651–1659.
[54] X. Wu, J. Lin, Z. Xu, C. Zhao, C. Lin, H. Wang, T. Lin, X. Zheng, B. Sa, Q. Zhang, Laser Photon. Rev. 15 (10) (2021), 2100211.
[55] M.G. García-Tecedor, Giulio Oropeza, Freddy Gómez, Laura liras, marta de la Peña, víctor antonio AntonioMorán, mariam Barawi, J. Mater. Chem. (2022).
[56] J. Li, X. Liu, P. Cui, J. Li, T. Ye, X. Wang, C. Zhang, Y.S. Zhao, Sci. China Chem. 62 (9) (2019) 1257–1262.
[57] J.S. Bechtel, J.C. Thomas, A. Van der Ven, Phys. Rev. Mater. 3 (11) (2019), 113605.
[58] K.M. Hossain, M.Z. Hasan, M.L. Ali, Results Phys. 19 (2020), 103337.
[59] A. Suzuki, T. Oku, Appl. Surf. Sci. 483 (2019) 912–921.
[60] T. Ouahrani, F.-Z. Medjdoub, S. Gueddida, Á.L. Fernandez, R. Franco, N.-E. Benkhettou, M. Badawi, A. Liang, J. Gonzalez, D. Errandonea, J. Phys. Chem. C 125 (1) (2020) 107–119.
[61] W. Ning, X.G. Zhao, J. Klarbring, S. Bai, F. Ji, F. Wang, S.I. Simak, Y. Tao, X.M. Ren, L. Zhang, Adv. Funct. Mater. 29 (10) (2019), 1807375.
[62] J. Huang, M. Lai, J. Lin, P. Yang, Adv. Mater. 30 (48) (2018), e1802856.
[63] T.G. Liashenko, E.D. Cherotchenko, A.P. Pushkarev, V. Pakštas, A. Naujokaitis, S.A. Khubezhov, R.G. Polozkov, K.B. Agapev, A.A. Zakhidov, I.A. Shelykh, Phys. Chem. Chem. Phys. 21 (35) (2019) 18930–18938.
[64] J. Deng, H. Lai, M. Chen, M. Glen, S. Wen, B. Zhao, Z. Liu, H. Yang, M. Liu, L. Huang, Miner. Eng. 136 (2019) 168–174.
[65] M. Benedikter, J. Musso, M.K. Kesharwani, K.L. Sterz, I. Elser, F. Ziegler, F. Fischer, B. Plietker, W. Frey, J. Kästner, ACS Catal. 10 (2020) 14810–14823.
[66] T. Yousef, J. Mol. Struct. 1215 (2020), 128180.
[67] J.H. Lee, S.H. Kim, K.Y. Doh, E.H. Kim, D. Lee, J. Am. Chem. Soc. 142 (35) (2020) 14859–14863.
[68] B. Indrajit Sharma, J. Maibam, R. Paul, R. Thapa, R. Brojen Singh, Indian J. Phys. 84 (6) (2010) 671–674.
[69] A. Soltani, R. Mashkoor, A. Khalaji, S. Raz, S. Ghoran, M. Dusek, K. Fejfarova, Y. Kanani, J. Struct. Chem. 60 (6) (2019) 890–897.
[70] H. Shou, R. Xie, M. Peng, Y. Duan, Y. Sun, Phys. B Condens. Matter 560 (2019) 41–45.
[71] S. Hussain, R. Hussain, M.Y. Mehboob, S.A.S. Chatha, A.I. Hussain, A. Umar, M.U. Khan, M. Ahmed, M. Adnan, K. Ayub, ACS Omega 5 (13) (2020) 7641–7650.
[72] C. Liu, Y. Li, Q. Cheng, Y.J.M. Zhao, Minerals 12 (3) (2022) 387.
[73] I.V. Yudanov, A. Genest, S. Schauermann, H.J. Freund, N. Rosch, Nano Lett. 12 (4) (2012) 2134–2139.
[74] H. Shiiba, N. Zettsu, M. Nakayama, S. Oishi, K. Teshima, J. Phys. Chem. C 119 (17) (2015) 9117–9124.
[75] S.Y. Kim, S.J. Cho, S.E. Byeon, X. He, H.J. Yoon, Adv. Energy Mater. 10 (44) (2020), 2002606.
[76] Z. Yang, B.H. Babu, S. Wu, T. Liu, S. Fang, Z. Xiong, L. Han, W. Chen, Solar Rrl 4 (2) (2020), 1900257.
[77] K. Choi, H. Choi, J. Min, T. Kim, D. Kim, S.Y. Son, G.-W. Kim, J. Choi, T. Park, Solar RRL 4 (2) (2020), 1900251.
[78] J. Qi, X. Yang, P.Y. Pan, T. Huang, X. Yang, C.C. Wang, W. Liu, Environ. Sci. Technol. 56 (8) (2022) 5200–5212.
[79] K. Zhou, W. Ma, Z. Zeng, X. Ma, X. Xu, Y. Guo, H. Li, L. Li, Chem. Eng. J. 372 (2019) 1122–1133.
[80] A.H. Mashhadzadeh, M. Fathalian, M.G. Ahangari, M. Shahavi, Mater. Chem. Phys. 220 (2018) 366–373.
[81] H. Wei, Y. Gui, J. Kang, W. Wang, C. Tang, Nanomaterials 8 (9) (2018) 646.
[82] K. Li, N. Li, N. Yan, T. Wang, Y. Zhang, Q. Song, H. Li, Appl. Surf. Sci. 515 (2020), 146028.
[83] C.C. Lin, S.K. Huang, C.E. Hsu, Y.C. Huang, C.Y. Wei, C.Y. Wen, S.S. Li, C.W. Chen, C.C. Chen, J. Phys. Chem. Lett. 11 (9) (2020) 3287–3293.
[84] P. Nekvindova, J. Cajzl, A. Mackova, P. Malinský, J. Oswald, R. Boettger, R. Yatskiv, J. Alloys Compd. 816 (2020), 152455.
[85] J. Zhu, K. Yang, Y. Chen, G. Fan, L. Zhang, B. Guo, X. Guan, R. Zhao, J. Hazard Mater. 409 (2021), 124504.
[86] Y. Cai, J. Cui, M. Chen, M. Zhang, Y. Han, F. Qian, H. Zhao, S. Yang, Z. Yang, H. Bian, T. Wang, K. Guo, M. Cai, S. Dai, Z. Liu, S. Liu, Adv. Funct. Mater. 31 (7) (2020).
[87] P.P. Murmu, V. Karthik, Z. Liu, V. Jovic, T. Mori, W.L. Yang, K.E. Smith, J.V. Kennedy, ACS Appl. Energy Mater. 3 (10) (2020) 10037–10044.
[88] L. Yan, M. Wang, C. Zhai, L. Zhao, S. Lin, Interfaces, ACS Appl. Mater. 12 (36) (2020) 40453–40464.
[89] Y. Bai, X. Meng, S. Yang, Adv. Energy Mater. 8 (5) (2018), 1701883.
[90] E. Mosconi, B. Merabet, D. Meggiolaro, A. Zaoui, F. De Angelis, J. Phys. Chem. C 122 (25) (2018) 14107–14112.
[91] M.M. Tavakoli, M. Saliba, P. Yadav, P. Holzhey, A. Hagfeldt, S.M. Zakeeruddin, M. Grätzel, Adv. Energy Mater. 9 (1) (2019), 1802646.
[92] R. Zeng, K. Bai, Q. Wei, T. Chang, J. Yan, B. Ke, J. Huang, L. Wang, W. Zhou, S. Cao, Nano Res. 14 (5) (2021) 1551–1558.
[93] M. Zhang, X. Chen, J. Xiao, M. Tai, D. Legut, J. Shi, J. Qu, Q. Zhang, X. Li, L. Chen, R. Zhang, H. Lin, Q. Zhang, Nanoscale 12 (11) (2020) 6571–6581.
[94] Y. Zhang, Z. Wang, S. Hu, P. Yan, H. Li, C. Sheng, ACS Appl. Mater. Interfaces 13 (10) (2021) 12042–12048.
[95] K.-L. Wang, Y.-G. Yang, Y.-H. Lou, M. Li, F. Igbari, J.-J. Cao, J. Chen, W.-F. Yang, C. Dong, L. Li, R.-Z. Tai, Z.-K. Wang, eScience 1 (1) (2021) 53–59.
[96] E.K. Barimah, A. Boontan, D.P. Steenson, G. Jose, Sci. Rep. 12 (1) (2022), 11421.
[97] S. Cao, S. Zhang, T. Zhang, Q. Yao, J.Y. Lee, Joule 3 (4) (2019) 1152–1162.
[98] M. Wu, Y. Shi, R. Li, P. Wang, ACS Appl. Mater. Interfaces 10 (46) (2018) 39819–39827.
[99] X. Xiao, D. Shi, Z. Yang, Q. Yu, D. Kaneko, M. Chen, New J. Chem. 45 (8) (2021) 4016–4023.
[100] S. Yang, G. Lei, H. Xu, B. Xu, H. Li, Z. Lan, Z. Wang, H. Gu, Appl. Surf. Sci. 480 (2019) 205–211.
[101] A. Sahinovic, B. Geisler, Phys. Rev. Res. 3 (4) (2021).